International Journal of Multiphase Flow 34 (2008) 966–986

Contents lists available at ScienceDirect

International Journal of Multiphase Flow

journal homepage: www.elsevier.com/locate/ijmulflow

Lateral migration of a capsule in a plane Poiseuille flow in a channel

Sai K. Doddi, Prosenjit Bagchi *

Department of Mechanical and Aerospace Engineering, Rutgers University, The State University of New Jersey, 98 Brett Road, Piscataway, NJ 08854, USA

ARTICLE INFO

Article history:
Received 30 December 2006
Received in revised form 6 February 2008
Available online 21 March 2008

ABSTRACT

Three-dimensional numerical simulation is presented on the motion of a deformable capsule undergoing large deformation in a plane Poiseuille flow in a channel at small inertia. The capsule is modeled as a liquid drop surrounded by an elastic membrane which follows neo-Hookean law. The numerical methodology is based on a mixed finite-difference/Fourier transform method for the flow solver and a front-tracking method for the deformable interface. The methodology can address large deformation of a capsule over a wide range of capsule-to-medium viscosity ratio. An extensive validation of the methodology is presented on capsule deformation in linear shear flow and compared with the boundary-element/integral simulations. Motion of a capsule in wall-bounded parabolic flow is simulated over an extended period of time to consider both transient and steady-state motion. Lateral migration of the capsule towards the centerline of the channel is observed. Results are presented over a range of capillary number, viscosity ratio, capsule-to-channel size ratio, and lateral location. After an initial transient phase during which the capsule deforms very quickly, the flow of the capsule is observed to be a quasi-steady process irrespective of capillary number (Ca), capsule-to-channel size ratio (a/H), and viscosity ratio (λ). Migration velocity and capsule deformation are observed to increase with increasing Ca and a/H, but decrease with increasing λ, and increasing distance from the wall. Numerical results on the capsule migration are compared with the analytical results for liquid drops, and capsules with Hookean membrane which are valid in the limit of small deformation. Unlike the prediction for liquid drops, capsules are observed to migrate toward the centerline for $0.2 \leqslant \lambda \leqslant 5$ range considered here. The migration velocity is observed to depend linearly on $(a/H)^3$, in agreement with the small-deformation theory, but non-linearly on Ca and the distance from the wall, in violation of the theory. Using the present numerical results and the analytical results, we present a correlation that can reasonably predict migration velocity of a capsule for moderate values of a/H and Ca.

1. Introduction

Capsules are liquid drops surrounded by thin elastic membranes. Many biological cells, such as erythrocytes and leukocytes, are often modeled as capsules (Pozrikidis, 2003, 2005; Marella and Udaykumar, 2004). Artificial capsules are also abundant in industrial applications related to food and polymer processing (Borhan and Gupta, 2003; Gutcho et al., 1979).

Dynamics of capsules in shear flow has been studied for several decades using analytical, numerical and experimental techniques. When placed in a shear flow, a capsule deforms and aligns itself with the flow, as does a liquid drop. However, unlike in a liquid drop, properties of the membrane material play a critical role in the dynamics of the capsule. Deformation of a capsule suspended in a shear flow was measured by Chang and Olbright (1993). Rehage et al. (2002) measured the deformation of a polyamide membrane capsule in a linear shear flow and showed that deformation increased linearly at low shear rates, but non-linearly at higher shear rates. Deformation and shape instability of a capsule with organosiloxane membrane were measured by Walter et al. (2001). Recently, Risso et al. (2006) experimentally investigated single-file motion of artificial capsules flowing through narrow tubes.

The pioneering works of Barthes-Biesel and co-workers (Barthes-Biesel, 1980; Barthes-Biesel and Rallison, 1981; Barthes-Biesel and Sgaier, 1985) led to the development of the theory of small deformation of a capsule suspended in a shear (or, a general linear) flow. Li et al. (1988) computed axisymmetric large deformation of capsules in a straining flow, and Leyrat-Maurin and Barthes-Biesel (1994) studied axisymmetric large deformation of a capsule during its passage through a hyperbolic constriction. Queguiner and Barthes-Biesel (1997) studied the axisymmetric motion of capsules through cylindrical tubes. Pozrikidis (1995), and Ramanujan and Pozrikidis (1998) used boundary integral simulation to consider large deformation of capsules in shear flow. Pozrikidis (2001), and Kwak and Pozrikidis (2001) have also studied the effect of membrane bending resistance on the deformation of a capsule suspended in shear flow and in axisymmetric straining flow. Effect

* Corresponding author.
E-mail address: pbagchi@jove.rutgers.edu (P. Bagchi).

0301-9322/$ - see front matter © 2008 Elsevier Ltd. All rights reserved.
doi:10.1016/j.ijmultiphaseflow.2008.03.002

of membrane viscosity on the dynamic response of a capsule was studied by Diaz et al. (2000, 2001). Capsule deformation under various constitutive laws for the membrane material was studied by Barthes-Biesel et al. (2002), and Lac et al. (2004). Using bicubic B-splines for surface discretization in conjunction with boundary-element method, Lac et al. (2004) showed that at higher membrane stiffness (or, low shear rate), the capsule shape becomes unstable for neo-Hookean membranes in absence of a bending resistance. Effect of membrane pre-stress was studied by Lac and Barthes-Biesel (2005). Barthes-Biesel and Chim (1981) studied the rheology of a dilute suspension of capsules at small deformation. Breyiannis and Pozrikidis (2000) considered suspension of two-dimensional capsules in shear flow. In a recent work, Lac et al. (2007) numerically studied the interaction between a pair of capsules in shear flow.

Capsules suspended in a liquid flowing through conduits are often encountered in many biological processes, and in biomedical devices. Examples are the motion of blood cells through blood vessels, flow chambers, and cell separation devices. In a wall-bounded shear flow, the motion of a capsule (and liquid drop) is characterized by its migration lateral to the wall. Lateral migration of liquid drops or capsules plays an important role during the flow of a suspension of particles in which case a particle-free region is developed near the wall. Reduced local viscosity in the particle-free region helps reducing the resistance to flow in small vessels, and is critical for blood flow in microcirculation.

Lateral migration of liquid drops has been a subject of investigation for many years. Here we briefly discuss a few studies on the migration of liquid drops. In the limit of zero inertia, a liquid drop moves laterally in a wall-bounded shear flow due to the asymmetry introduced by the deformation of the particle by the imposed shear. A liquid drop in a linear shear flow bounded by a single wall continues to migrate away from the wall, whereas in a wall-bounded parabolic flow, it settles at the centerline or in between the centerline and a wall. Experimental studies on drop motion in wall-bounded shear flow have been carried out by Karnis et al., 1963, Goldsmith and Mason (1962), Karnis and Mason (1967), Chan and Leal (1981), Hiller and Kowalewski (1987), and Smart and Leighton (1991), among others. Early theoretical works on drop migration in presence of wall in the limit of small deformation have been considered by Chaffey et al. (1967), Ho and Leal (1974), and others (see, e.g. Chan and Leal, 1981, for a review). Chaffey et al. (1967) predicted that the lateral velocity of a droplet in a wall-bounded linear shear flow decreases inversely with the square of the distance from the wall. Chan and Leal (1979) extended the small deformation analysis to drop migration in wall-bounded Couette and plane parabolic flows. For a Newtonian drop suspended in a parabolic flow of another Newtonian fluid, their results showed that the drop migrates away from the wall and settles at the centerline for drop-to-medium viscosity ratio (λ) of less than unity. But for $\lambda \sim O(1)$, it settles at a position between the wall and the axis. Using the method of reflections, Shapira and Haber (1988) obtained an approximate expression of the deformation and drag force on a drop moving parallel to a wall in a quiescent fluid bounded by two walls. The wall effects on the drop deformation was shown to be greater for drops located close to the walls, and to vanish for drops moving along the centerline. Shapira and Haber (1990) extended the analysis to Couette flow in presence of a wall. Uijttewaal et al. (1993) used boundary integral method to study drop deformation and migration in linear shear flow in presence of a wall, and observed large deviations from the theory of Chan and Leal (1979), and Shapira and Haber (1988, 1990) at small wall distances and large drop deformation. Uijttewaal and Nijhof (1995) extended the boundary integral method to consider viscosity ratios other than unity. Coulliette and Pozrikidis (1998) studied transient motion of three-dimensional liquid drops in cylindrical tubes at $\lambda = 1.0$ using boundary integral simulation, and observed migration towards the tube center. Li and Pozrikidis (2000) also considered wall-bounded shear flow and plane Poiseuille channel flow of two-dimensional suspensions of liquid drops. Recently, Griggs et al. (2007) formulated an efficient three-dimensional boundary-integral method for motion of deformable drops between two parallel walls that can consider a wide range of capillary number, drop-to-channel size ratio, and drop-to-medium viscosity ratio.

In the case of a finite Reynolds number liquid drop, the effect of inertia and drop deformation both contribute to lateral migration. Mortazavi and Tryggvason (2000) showed that in presence of high inertia, an isolated liquid drop undergoes a transient oscillatory motion about its equilibrium position, and a steady-state may not be achieved at sufficiently high Reynolds number.

In the limit of a rigid spherical particle, lateral migration is possible only in presence of inertia, and an extensive literature exists on this subject. Here we avoid the discussion on the subject, and refer to a recent article by Magnaudet et al. (2003) which provides an excellent review of the topic.

Unlike liquid drops, capsule migration in wall-bounded shear flow is relatively less studied. Experiments performed by Goldsmith (1971) using dilute suspensions of red blood cells showed center-ward migration, similar to the case of liquid drops. Extending the theory of small deformation, Helmy and Barthes-Biesel (1982) studied the migration of a capsule in an unbounded parabolic flow, and showed that similar to a liquid drop, an isolated capsule migrates laterally toward the centerline due to its deformation under external shear. Pozrikidis (2005) presented boundary-element simulation of spherical, oblate ellipsoidal and biconcave capsules in tube flow, and observed that spherical capsules slowly migrate towards the tube centerline, and oblate and biconcave capsules developed parachute and slipper-like shapes, respectively.

In this article we present a numerical method for large deformation of three-dimensional capsules which is based on a mixed finite-difference/Fourier transform method for the flow solver and a front-tracking method for deformable interfaces. Capsules are modeled as liquid drops surrounded by elastic membranes which follow neo-Hookean law. Extensive validation of the methodology is presented on capsule deformation in linear shear flow and compared with the boundary integral simulation of Lac et al. (2004), and Ramanujan and Pozrikidis (1998). Capsule migration in wall bounded parabolic flow is simulated over an extended period of time to consider both transient and steady-state migration. The capsules are released off the channel centerline, and hence the problem is essentially non-axisymmetric. Results are presented over a range of capillary number, viscosity ratio, capsule to channel size ratio, and lateral location.

2. Flow configuration and simulation technique

2.1. Problem setup

The flow configuration is described in Fig. 1. We consider the motion of an array of capsules in a channel bounded by two infinite flat plates placed parallel to the X-axis in the XYZ coordinate system as shown. The height of the channel is H. The separation between adjacent capsules in the X direction is denoted by L_{x0} and in the Z direction by L_{z0}. The fluids, inside and outside of the capsules, are incompressible and Newtonian. The fluids have same density but may differ in viscosity. Viscosity of the liquid interior of the capsule is denoted by μ_c, while that of the external liquid is μ_0. In absence of the capsules, the undisturbed flow $\mathbf{u}_0$ is a fully-developed parabolic (Poiseuille) flow, and is directed from

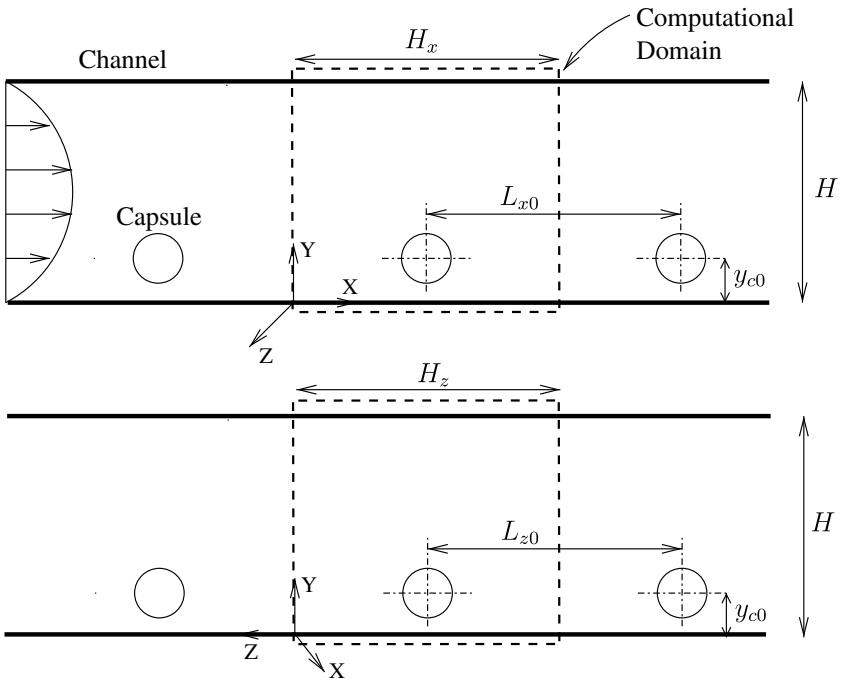

Fig. 1. Schematic of the flow configuration. The computational domain is indicated by dashed lines.

$X = -\infty$ to $X = +\infty$, and is driven by a constant pressure gradient $\mathrm{d}P/\mathrm{d}X$ as

$$\mathbf{u}_0 = \left[\frac{1}{2\mu_0}\left(-\frac{\mathrm{d}P}{\mathrm{d}X}\right)(HY - Y^2),\ 0,\ 0\right]. \tag{1}$$

Here Z is the direction of vorticity of the undisturbed flow. The capsules are released in this flow at time $t = 0$ off the center of the channel. The initial location of the capsule centroid is denoted by X_{c0}, Y_{c0}, Z_{c0}, which are varied in the simulations as described later.

2.2. Boundary conditions

At the top and bottom walls (Fig. 1), no-slip conditions are imposed as

$$\mathbf{u} = [0, 0, 0], \quad \text{at } Y = 0 \text{ and } H. \tag{2}$$

Since the channel and the capsule array are infinitely long in the X and Z directions, one can use periodicity condition in these directions to reduce the size of the computational domain. The computational domain is shown in Fig. 1 by dashed lines. The streamwise length of the domain is H_x and the length in the Z direction is H_z. As discussed later, the condition of periodicity not only reduces the size of the domain, but also allows us to use Fourier transform for fast computation.

2.3. Fluid–structure interaction

The simulation technique considered here is the front-tracking/immersed boundary method (Peskin et al., 1977; Unverdi and Tryggvason, 1992; Tryggvason et al., 2001) for multiple fluids with different properties. The main idea of the front-tracking method is to use a single set of equations for both the fluids, inside and outside of the capsule. The fluid equations are solved on a fixed Eulerian grid, and the interface is tracked in a Lagrangian manner by a set of marker points (Fig. 2). The interface is accounted for by introducing a body force $\mathbf{F}(\mathbf{x}, t)$ in the governing equations such that it is zero everywhere in the flow except at the interface:

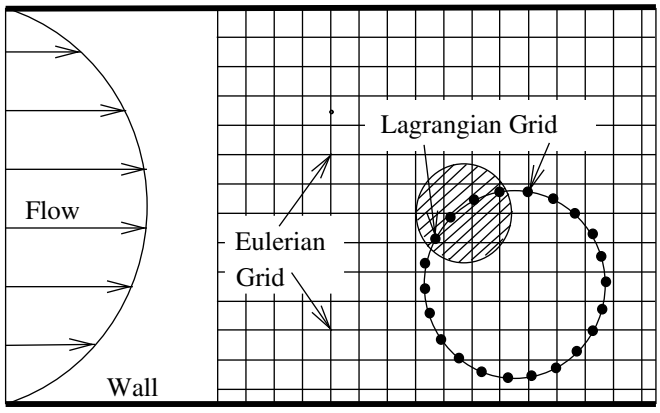

Fig. 2. The Eulerian and Lagrangian grids.

$$\mathbf{F}(\mathbf{x}, t) = \int_{\partial S} \mathbf{f}(\mathbf{x}', t)\delta(\mathbf{x} - \mathbf{x}')\,\mathrm{d}\mathbf{x}', \tag{3}$$

where $\mathbf{x}$ is the location of an arbitrary point in the flow domain, $\mathbf{x}'$ is any point on the interface, ∂S is the entire interface, and δ is the three-dimensional Delta function which vanishes everywhere except at the interface. Here $\mathbf{f}$ is the elastic force generated in the membrane due to deformation of the capsule. For incompressible fluids of different viscosity, the governing equations are:

$$\nabla \cdot \mathbf{u} = 0, \quad \text{and} \quad \rho\left[\frac{\partial \mathbf{u}}{\partial t} + \mathbf{u} \cdot \nabla \mathbf{u}\right] = -\nabla p + \nabla \cdot \tau + \mathbf{F}. \tag{4}$$

Here $\mathbf{u}(\mathbf{x}, t)$ is the fluid velocity, ρ is the density, p pressure, and

$$\tau = \mu(\nabla \mathbf{u} + (\nabla \mathbf{u})^{\mathrm{T}}) \tag{5}$$

is the viscous stress tensor. Here $\mu(\mathbf{x}, t)$ is the viscosity in the entire fluid: within a capsule, $\mu = \mu_c$, and for any point outside, $\mu = \mu_0$. As the capsules move and deform, $\mu(\mathbf{x}, t)$ needs to be updated. Following Tryggvason et al. (2001), this is done by solving a Poisson equation for an indicator function $I(\mathbf{x})$ such that

$$\mu(\mathbf{x}) = \mu_0 + (\mu_c - \mu_0)I(\mathbf{x}). \tag{6}$$

The δ function used in (3) is constructed by multiplying three 1D δ functions as

$$\delta(\mathbf{x} - \mathbf{x}') = \delta(x - x')\delta(y - y')\delta(z - z'). \tag{7}$$

For numerical implementation, a smooth representation of the δ-function is used as

$$D(\mathbf{x} - \mathbf{x}') = \frac{1}{64\Delta^3}\prod_{i=1}^{3}\left(1 + \cos\frac{\pi}{2\Delta}(x_i - x_i')\right) \quad \text{for } |x_i - x_i'| \leqslant 2\Delta, \quad i = 1,2,3,$$
$$D(\mathbf{x} - \mathbf{x}') = 0 \quad \text{otherwise}, \tag{8}$$

where Δ is the Eulerian grid size (Unverdi and Tryggvason, 1992). As a result, the membrane force and viscosity vary smoothly over four Eulerian grid points surrounding the interface. In discrete form, the integral in (3) can be written as

$$\mathbf{F}(\mathbf{x}_j) = \Sigma_i D(\mathbf{x}_j - \mathbf{x}_i')\mathbf{f}(\mathbf{x}_i'), \tag{9}$$

where i and j represent Lagrangian and Eulerian points, respectively.

2.4. Numerical treatment of membrane deformation

The capsule membrane follows the neo-Hookean law for which the strain energy function is given by

$$W = \frac{Eh}{6}(\epsilon_1^2 + \epsilon_2^2 + \epsilon_1^{-2}\epsilon_2^{-2} - 3), \tag{10}$$

where ϵ_1 and ϵ_2 are the principal strains, E is the elastic modulus, and h is the membrane thickness. The above equation describes a thin sheet of three-dimensional material with an elastic modulus of E, or equivalently, a two-dimensional membrane with a two-dimensional elastic modulus equal to Eh. We assume that the bending resistance of the membrane is negligible.

The deformation of the membrane is treated using a finite element model developed by Charrier et al. (1989), and Shrivastava and Tang (1993), and later implemented by Eggleton and Popel (1998) within the framework of immersed boundary method to consider large deformation of capsules. First, the membrane is discretized using flat triangular elements (Fig. 3a). A Lagrangian node on the surface is surrounded by five or six triangular elements. It is assumed that the elements remain flat even after large deformation of the capsule. In the model, the forces acting on the three vertices of a triangular element are obtained by computing the displacements of the vertices of the deformed element with respect to the undeformed element. For this purpose, the undeformed and deformed surface elements are transformed to a common plane P using rigid-body rotations (Fig. 3b). By denoting the three vertices of a triangular element as l, m, and n (see Fig. 3b), and the undeformed and deformed coordinates of the element as $\mathbf{x}$ and $\mathbf{X}$, respectively, the transformation rules used for coordinate rotation are

$$\mathbf{x}_l^P = \mathbf{0}, \quad \mathbf{x}_m^P = \mathbf{M}(\mathbf{x}_m - \mathbf{x}_l), \quad \mathbf{x}_n^P = \mathbf{M}(\mathbf{x}_n - \mathbf{x}_l), \quad \text{and} \tag{11}$$
$$\mathbf{X}_l^P = \mathbf{0}, \quad \mathbf{X}_m^P = \mathbf{R}(\mathbf{X}_m - \mathbf{X}_l), \quad \mathbf{X}_n^P = \mathbf{R}(\mathbf{X}_n - \mathbf{X}_l), \tag{12}$$

where $\mathbf{x}_l^P$, $\mathbf{X}_l^P$, etc. are the coordinates of the vertices of the undeformed and deformed elements on the common plane P; $\mathbf{M}$ and $\mathbf{R}$ are the transformation matrices defined as $M_{ij} = e_i^{\mathrm{u}} e_j^0$ and $R_{ij} = e_i^{\mathrm{d}} e_j^0$, where $\mathbf{e}^0, \mathbf{e}^{\mathrm{u}}$, and $\mathbf{e}^{\mathrm{d}}$ are the unit vectors attached to a fixed reference frame, to the undeformed element, and to the deformed element, respectively (Fig. 3b). Once the deformed and undeformed elements are transformed to the common plane P, the problem is reduced to a 2D (planar) deformation on $\{x^P, y^P\}$, where x^P, y^P denote a *local* coordinate system attached to the plane P. The displacements of the three vertices can be obtained which do not include

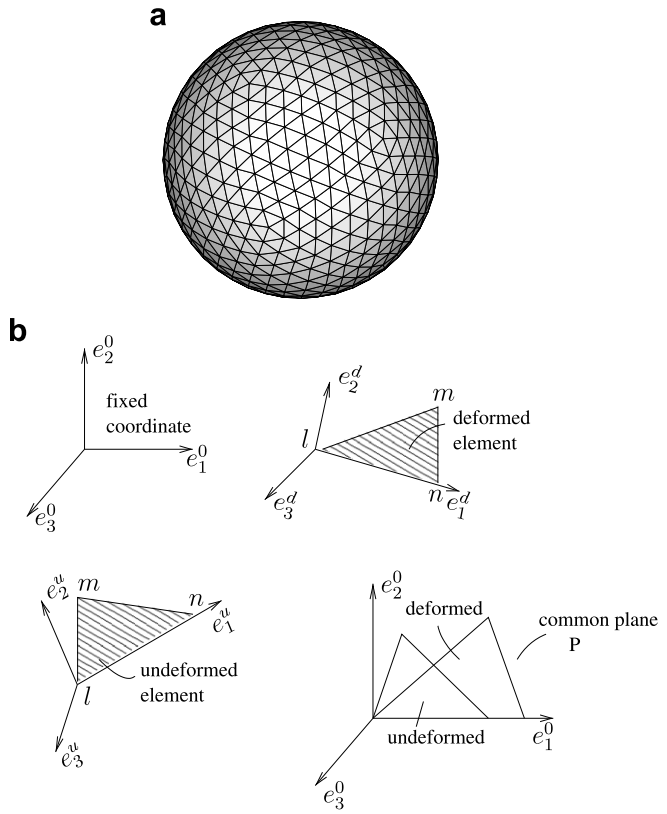

Fig. 3. (a) Lagrangian elements on the capsule surface. (b) Deformation of a planar triangular element in space, and comparison of the deformed and undeformed element in a common plane.

the contribution from a rigid-body rotation. Using the principle of virtual work, the forces in the common plane P are then obtained as

$$\mathbf{f}_l^P = \frac{\partial W}{\partial \epsilon_1}\frac{\partial \epsilon_1}{\partial \mathbf{v}_l} + \frac{\partial W}{\partial \epsilon_2}\frac{\partial \epsilon_2}{\partial \mathbf{v}_l} \tag{13}$$

for the vertex l, and similarly for vertices m and n. Here $\mathbf{v}$ is the displacement of a vertex, and ϵ_1 and ϵ_2 are the principal values of the in-plane stretch ratios. The force $\mathbf{f}^P$ lies in plane P.

We now assume that the displacement $\mathbf{v}$ varies linearly *inside* the element so that

$$\mathbf{v} = N_l\mathbf{v}_l + N_m\mathbf{v}_m + N_n\mathbf{v}_n. \tag{14}$$

and the shape functions N_l, N_m and N_n are expressed as

$$N_l = a_l x^P + b_l y^P + c_l \tag{15}$$

for the vertex l, and similarly for vertices m and n. The coefficients a_l, etc. are found by letting $N_l = 1$ at vertex l, and $N_l = 0$ at vertices m and n, and so on. Once the shape functions are known, the displacement gradients within the element, such as $\partial\mathbf{v}/\partial x^P$, and $\partial\mathbf{v}/\partial y^P$, can be found by differentiating (14).

At this point we need to express the in-plane stretch ratios ϵ_1 and ϵ_2 in terms of the gradients $\partial\mathbf{v}/\partial x^P$ etc, in order to evaluate the derivatives in (13). For a planar deformation, ϵ_1 and ϵ_2 can be related to the deformation gradient tensor $\mathbf{D}$ as

$$\epsilon_1^2 = \frac{1}{2}\left[G_{11} + G_{22} + \sqrt{\{(G_{11} - G_{22})^2 + 4G_{12}^2\}}\right], \tag{16}$$
$$\epsilon_2^2 = \frac{1}{2}\left[G_{11} + G_{22} - \sqrt{\{(G_{11} - G_{22})^2 + 4G_{12}^2\}}\right], \tag{17}$$

where $\mathbf{G} = \mathbf{D}^{\mathrm{T}}\mathbf{D}$ is a symmetric positive definite matrix. Using the expressions for $\partial\mathbf{v}/\partial x^P$, and $\partial\mathbf{v}/\partial y^P$, the components of $\mathbf{G}$ can be written explicitly in terms of the shape functions N and the nodal

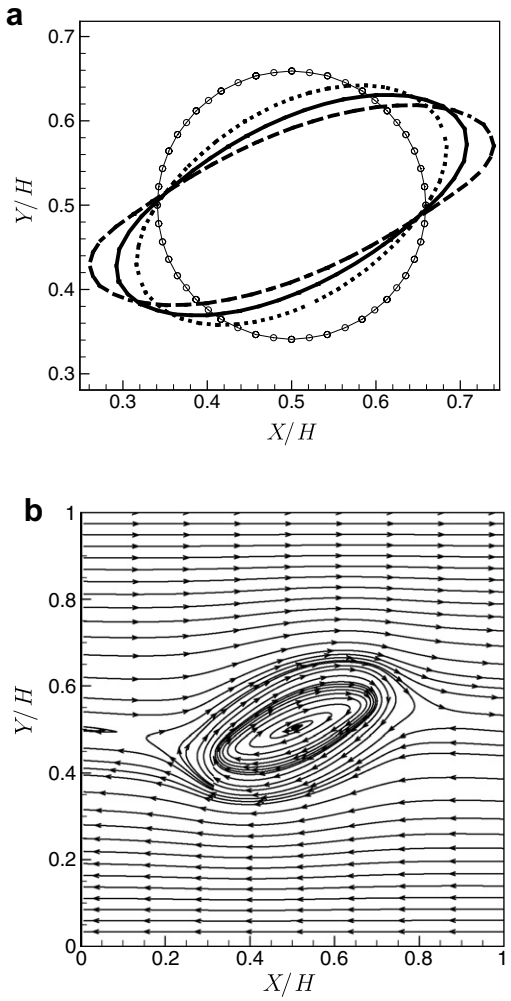

Fig. 4. (a) Capsule deformation in linear shear flow. 2D shapes in the shear plane are shown after steady state is reached. –○– Initial shape, ····· $Ca = 0.05$, – – – $Ca = 0.1$, – – – $Ca = 0.2$. (b) Flow field at $Ca = 0.1$ after steady state is reached.

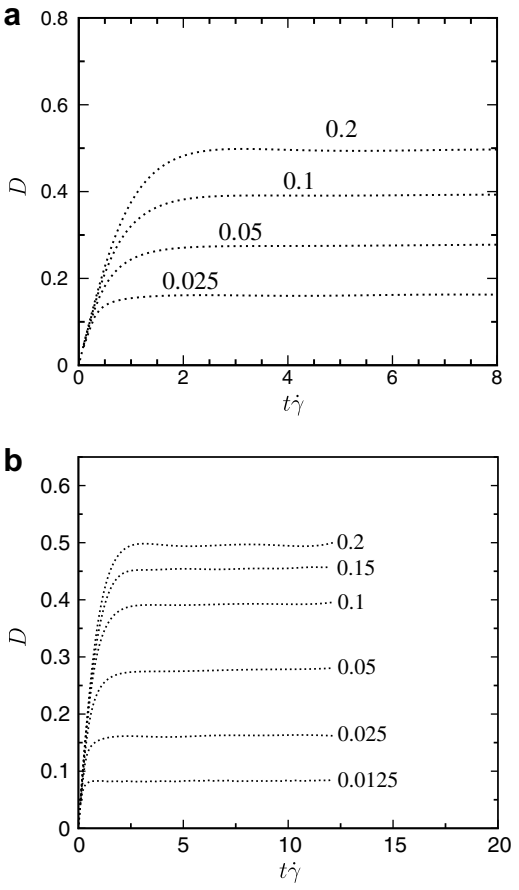

Fig. 5. Validation of the numerical methodology: Deformation parameter D versus time. ····· Present results. (a) —— Ramanujan and Pozrikidis (1998). (b) —— Lac et al. (2004). Values next to the curves indicate capillary numbers. In order to obtain the curves from RP and L1, the figures in their papers were scanned and then uploaded in Tecplot.

displacement **v**. The derivatives in (13), such as $\partial\epsilon_1/\partial\mathbf{v}$, can then be written explicitly, and hence $\mathbf{f}^P$ can be evaluated at each of the vertices of an element. Once the in-plane forces for individual element are found, they need to be transformed to the global coordinates. This is done by using the transformation rule $\mathbf{f} = \mathbf{R}^{\mathrm{T}}\mathbf{f}^P$, where **R** is the transformation matrix as explained above. The resultant force $\mathbf{f}(\mathbf{x}', t)$ at any node is obtained by vector resultant of the forces contributed by all the elements which share that node.

2.5. Interface tracking

The capsule membrane is tracked in a Lagrangian manner. The velocity of the interface is computed at each time step, after solving the Navier–Stokes equations, as

$$\mathbf{u}(\mathbf{x}') = \int_S \mathbf{u}(\mathbf{x})\delta(\mathbf{x} - \mathbf{x}')\,\mathrm{d}\mathbf{x}, \tag{18}$$

where S indicates the entire flow domain. Though the summation is over all Eulerian nodes, only the 'local' nodes contribute to the membrane velocity. The discrete form of the delta function used here is the same given by (8). In this way, a weighted interpolation of the Eulerian fluid velocity is performed which ensures that the continuity of velocity across the membrane is satisfied. The Lagrangian points on the membrane are then advected as

Table 1
Validation: comparison of steady state deformation D with Ramanujan and Pozrikidis (1998) (RP), Lac et al. (2004) (L1), Li and Sarkar (2008) (LS) and small deformation theory (SD) of Barthes-Biesel and Rallison (1981)

Ca	Present	RP	L1	SD	LS
0.0125	0.083			0.08	
0.025	0.162	0.16	0.15	0.16	
0.05	0.278	0.27	0.27	0.32	
0.1	0.392	0.39	0.40	0.63	0.37
0.15	0.460		0.47		
0.2	0.496	0.5	0.52		0.49

In order to obtain the data from RP and L1, their curves were first scanned and then uploaded in Tecplot. L1's data at $Ca = 0.0125$ was not clearly visible and hence not reported.

$$\frac{\mathrm{d}\mathbf{x}'}{\mathrm{d}t} = \mathbf{u}(\mathbf{x}'). \tag{19}$$

Numerically, above equation is treated explicitly using the second-order Adams–Bashforth scheme as

$$\mathbf{x}'_{n+1} = \mathbf{x}'_n + \Delta t\left[\frac{3}{2}\mathbf{u}(\mathbf{x}'_n) - \frac{1}{2}\mathbf{u}(\mathbf{x}'_{n-1})\right], \tag{20}$$

where $n, n+1$, etc. are the time instances.

2.6. Dimensionless parameters

The centerline velocity of the undisturbed parabolic flow is U_{cl}. The undeformed shape of the capsule is spherical. The diameter of the capsule is denoted by a. The governing equations are made dimensionless using H as the characteristic length scale, U_{cl} as the velocity scale, and H/U_{cl} as the time scale. The dimensionless time is denoted by t^*. The major dimensionless parameters are: the capillary number $Ca = \mu_0 U_{cl}/Eh$ which is the ratio of the viscous force to the elastic force of the capsule membrane, the ratio of the viscosity of the interior fluid to that of the exterior fluid $\lambda = \mu_c/\mu_0$, and the size ratio a/H. The Reynolds number of the capsules, defined as $Re = \rho U_{cl} a/\mu_0$, is 0.01, and hence the effect of inertia is negligible. Other geometric parameters are the initial separation distance between the capsules, L_{x0}/H, and L_{z0}/H, in the x and z directions, respectively.

2.7. Flow solver

The governing equations are discretized spatially using a second-order finite difference scheme, and temporally using a two-step time-split scheme. In this method the momentum equation is split into an advection–diffusion equation and a Poisson equation for the pressure. The nonlinear term in the advection–diffusion equation is treated explicitly using a second-order Adams–Bashforth scheme, and the viscous terms are treated implicitly using the Crank–Nicholson scheme. The advection–diffusion equation is solved using an ADI (alternating direction implicit) scheme. The velocity is not divergence-free at the end of the advection–diffusion step. The Poisson equation is then solved to obtain pressure at the next time level. Using the new pressure, the velocity is corrected to make it divergence-free. In order to reduce computation, the Poisson equation is Fourier transformed in the x-direction yielding a set of 2D decoupled PDEs which is directly inverted to obtain pressure. Note that since the z-direction is periodic, the Poisson equation can be further reduced to 1D equations. In the code we have not implemented this as the 2D Poisson solver takes less computation time than the advection–diffusion step.

2.8. Numerical resolution

Typical Eulerian resolution used in this study is $120 \times 120 \times 120$, and Lagrangian resolution used is 1280 triangular elements. In some cases, e.g. for capsules with high Ca and for an array of closely-spaced capsules, we use 5120 triangular elements, and $160 \times 160 \times 160$ Eulerian points. Dimensionless timestep used in the simulation is 10^{-4}.

Table 2
Validation: comparison of capsule orientation θ/π at steady state with Ramanujan and Pozrikidis (1998) (RP), and Lac et al. (2004) (L1)

Ca	Present	RP	L1
0.0125	0.215		
0.025	0.201		0.2
0.05	0.168	0.17	0.17
0.1	0.136	0.14	0.14
0.15	0.121		0.12
0.2	0.107	0.11	0.10

RP's data at $Ca = 0.025$ is not included since θ did not reach a steady value in their simulation.

Table 3
Validation: comparison of tank–treading period $\dot{\gamma}T$, with Ramanujan and Pozrikidis (1998) (RP), and Lac et al. (2004) (L1)

Ca	Present[a]	Present[b]	RP	L1
0.025	14.1	13.4	13.4	13.0
0.05	16.2	15.0	14.6	14.9
0.1	19.0	17.8	16.6	17.8
0.15	20.9	20.0		19.6
0.2	22.2	21.3	19.7	22.1

[a]TTP is computed following a revolution of a marker point. [b]TTP is computed by integrating $\mathrm{d}l/|v|$ over the membrane circumference in the (x, y)-plane, as done in L1, where $\mathrm{d}l$ is a line segment of the capsule profile, and v is the membrane velocity.

3. Validation

3.1. Capsule deformation in linear shear flow

Before we present validation of our methodology, it should be mentioned that Eggleton and Popel (1998) previously used a similar IBM technique and the same numerical treatment for membrane deformation as described above to address large deformation of capsules in linear shear flow. Eggleton and Popel (1998) validated the methodology against the analytical results for small deformation of capsules obtained by Barthes-Biesel and Rallison (1981).

Before we present validation of our methodology, it should be mentioned that Eggleton and Popel (1998) previously used a similar

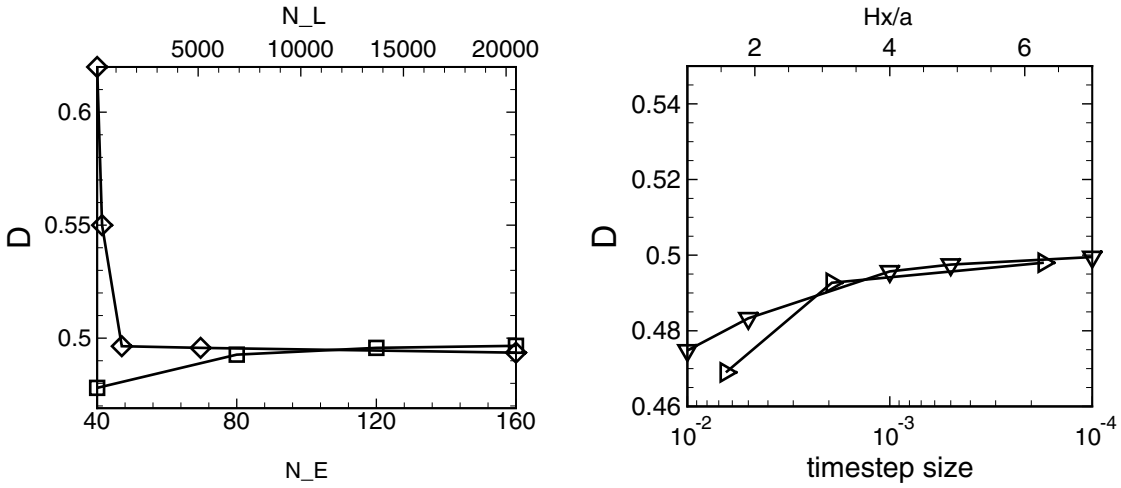

Fig. 6. Resolution tests at $Ca = 0.2$ showing the steady values of D. (a) Effects of varying Eulerian resolution $((N_E)^3)$ □, and Lagrangian resolution (N_L) ◇. N_L is the number of triangular elements on the capsule surface. (b) Effects of varying timestep size (Δt) ▽, and computational domain size (H_x) ▷.

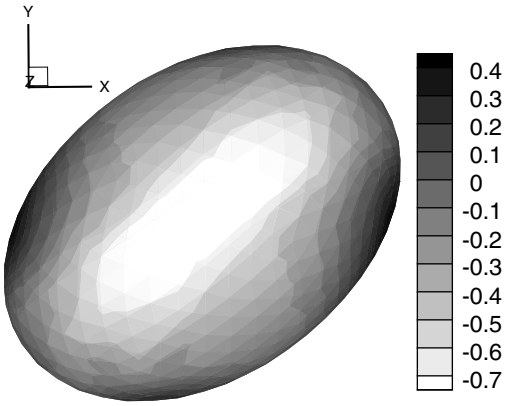

Fig. 7. Principal stress distribution for $Ca = 0.025$. Compressive (negative) stress (indicated by white shade) in the equatorial region can be seen.

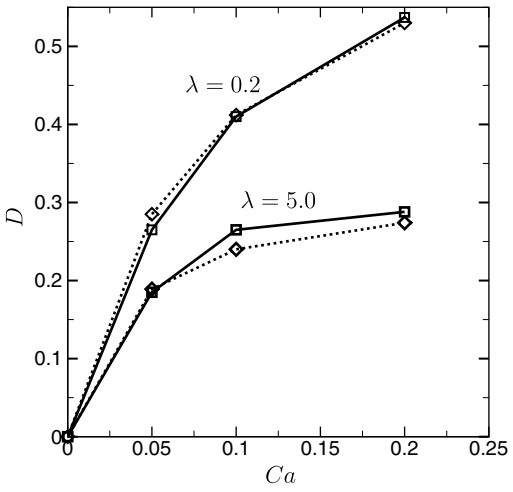

Fig. 8. Validation of the numerical methodology: Steady-state values of D for $\lambda \neq 1$. –□– Ramanujan and Pozrikidis (1998); ···◊··· present results.

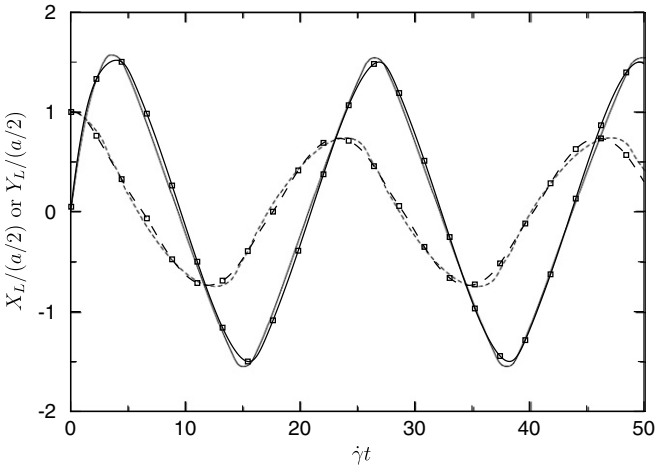

Fig. 9. Validation: Trajectory of a material point on the capsule membrane at $Ca = 0.2$. Solid line (x-coordinate); dashed line (y-coordinate). Lines without symbols are results from Lac et al. (2004). Lines with symbols are present results. Fig. 13b of L1 was scanned and then uploaded in Tecplot.

IBM technique and the same numerical treatment for membrane deformation as described above to address large deformation of

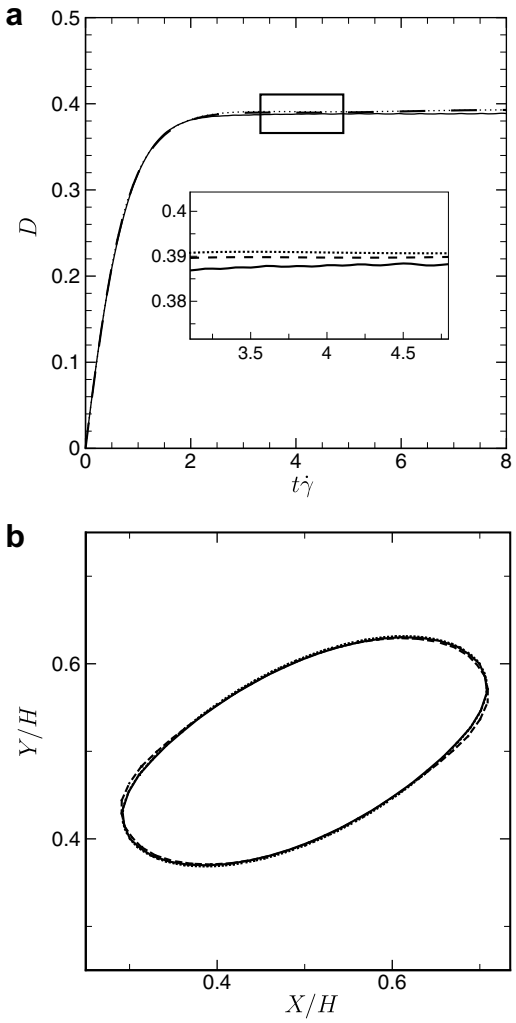

Fig. 10. Resolution test: (a) Deformation history, and (b) final steady shape in linear shear flow $Ca = 0.1$: ——, 80^3 Eulerian points and 1280 Lagrangian elements; – – – 120^3 Eulerian points and 1280 Lagrangian elements; ·····120^3 Eulerian points and 5120 Lagrangian elements. In (a), inset shows details.

capsules in linear shear flow. Eggleton and Popel (1998) validated the methodology against the analytical results for small deformation of capsules obtained by Barthes-Biesel and Rallison (1981).

We now present a series of validation of our present code. For this purpose, we consider deformation of an initially spherical capsule subject to a linear shear flow as

$$\mathbf{u}_0 = [\dot{\gamma}(Y - H/2), 0, 0], \tag{21}$$

where $\dot{\gamma}$ is the shear rate. The flow is bounded in the Y direction by two parallel walls which are placed H distance apart. The Z direction is the direction of vorticity. The no-slip condition is imposed at the top and bottom walls as

$$\mathbf{u} = \mathbf{u}_0(Y = 0, H). \tag{22}$$

Periodic conditions are imposed at the other boundaries of the domain as discussed in previous section. The computational domain for this problem is a cube with each side having length H. The capsule is placed at the middle ($X_{c0} = H/2, Y_{c0} = H/2, Z_{c0} = H/2$) of the computational domain. The capillary number for the shear flow problem is defined as $Ca = \dot{\gamma} a \mu_0 / 2Eh$.

Consider first $\lambda = 1$ case. The initially spherical capsule deforms in a shear flow and attains an ellipsoidal shape. The steady-state shape of the deformed capsule is shown in Fig. 4a as a function

of *Ca*. Capsule deformation increases, and it aligns more towards the *X*-axis with increasing *Ca*. This qualitative trend agrees with previous numerical results of Ramanujan and Pozrikidis (1998) (henceforth called RP) and Lac et al. (2004) (henceforth called L1). The flow field inside and around a deformed capsule is shown in Fig. 4b. The rotational motion of the fluid can be seen in the figure.

Quantitative comparisons with the results of RP and L1 are considered next. We consider time history of the deformation parameter, $D = (L - B)/(L + B)$ where L and B are the major and minor axis of the ellipsoid in the plane of the shear. Our results are compared with those of RP in Fig. 5a and of L1 in Fig. 5b. In Table 1, we list the numerical values of the steady-state deformation D obtained from our simulations, from RP, from L1, and also from small deformation analysis of Barthes-Biesel and Rallison (1981). We also compare our results with those of Li and Sarkar (2008) for $Ca = 0.1$ and 0.2, who used a similar but independently-developed front-tracking code to simulate capsule deformation. At low *Ca*, our results agree well with those predicted by the small deformation analysis. It should be noted that RP's results correspond to a zero-thickness shell, rather than a neo-Hookean membrane. RP mentioned that the resulting deformation is 4% less than the one that would be obtained with a neo-Hookean membrane. For $Ca \leqslant 0.1$, our front-tracking method predicts slightly higher values of D compared to those obtained by RP. For $Ca = 0.025, 0.05$, and 0.1, we predict 1.25%, 2.96%, and 0.5% higher values of D, respectively. For $Ca = 0.2$, we predict slightly lower (0.8%) value of D as compared to that of RP. In comparison to Lac et al., we predict higher values of D for $Ca < 0.1$; our prediction is 8%, and 2.96% higher for $Ca = 0.025$, and 0.05, respectively. In contrast, for $Ca \geqslant 0.1$, we predict lower values of D compared to those of Lac et al; our predicted values are 2%, 2.12%, and 4.6% less for $Ca = 0.1, 0.15$, and 0.2, respectively.

It is somewhat surprising that at higher *Ca*, we predicted less (though very small) D compared to that of RP. Before discussing the origin of these differences, we compare our results with those of Li and Sarkar (2008). Interestingly (and surprisingly), Li and Sarkar, similar to us, predicted lower deformation than those predicted by RP and Lac et al. Compared to the results obtained by Li and Sarkar, our results are closer to those of Lac et al., Li and Sarkar predicted 7.5%, and 5.8% less values of D compared to those predicted by Lac et al., for $Ca = 0.1$ and 0.2, respectively.

Extensive tests at $Ca = 0.2$ are done by varying Eulerian resolution (N_E), Lagrangian resolution (N_L), timestep size (Δt), and the size of the computational domain (H_x). The steady-state value of D with respect to these variables are shown in Fig. 6. In Fig. 6a, the effect of varying Eulerian resolution is shown. Capsule deformation increases with increasing Eulerian resolution, but reaches a converged solution for Eulerian resolution above 120^3. When the Eulerian resolution is changed from 40^3 to 80^3, D increases

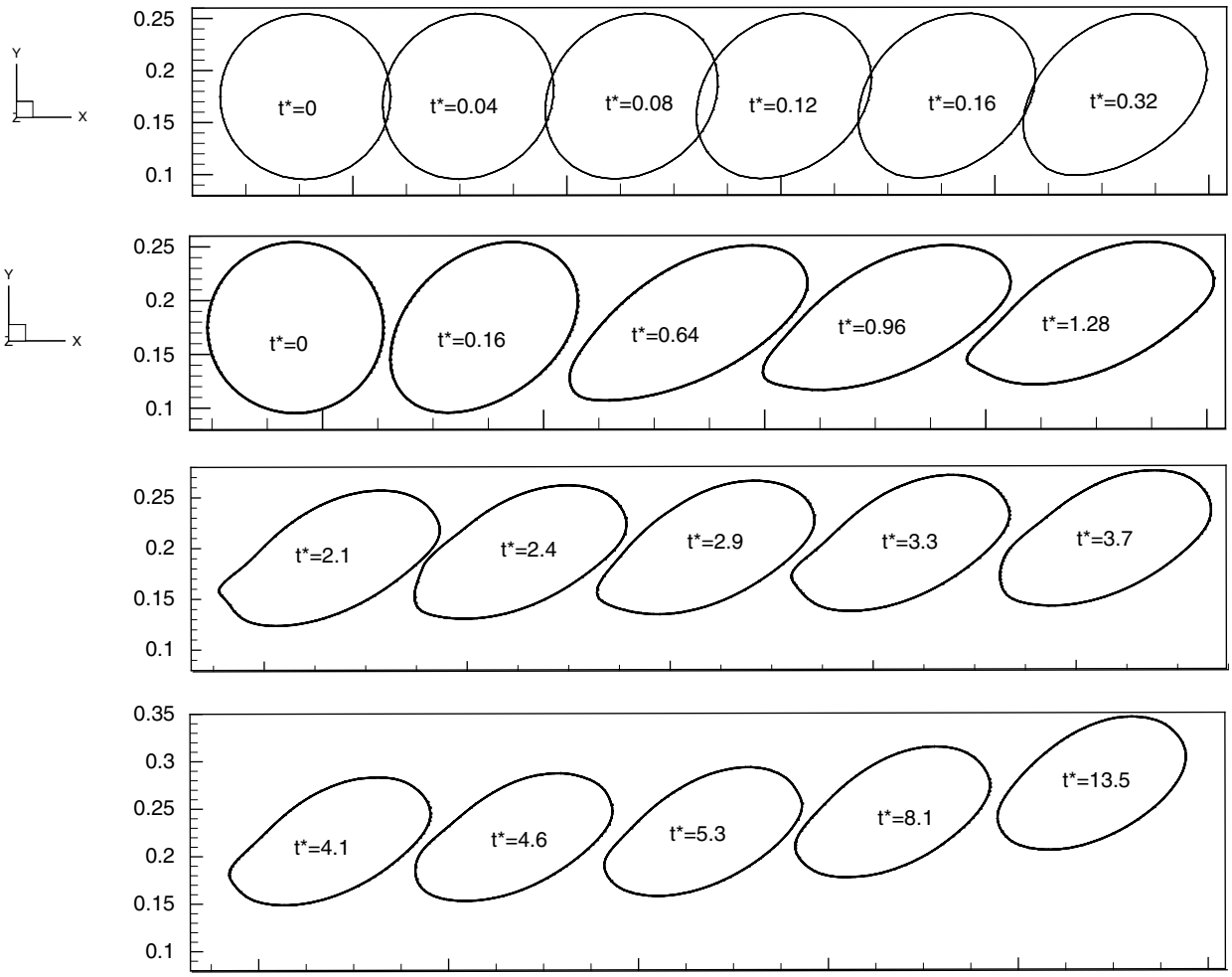

Fig. 11. Migration of a capsule in a pressure-driven flow in a channel. Sequence of capsule shapes during initial transience is shown for $Ca = 0.2$ (top row) and $Ca = 0.8$ (bottom three rows). Here $t^* = tU_{cl}/H$. X, Y, Z coordinates are scaled by channel height H. $Y/H = 0$ is bottom wall of the channel, and $Y/H = 0.5$ is channel center. Here $\lambda = 1$, and $a/H = 0.16$.

by 3.1%, but when the resolution is increased from 120^3 to 160^3, D increases by only 0.2%. Most of our simulations are done at 120^3 and some at 160^3. The effect of Lagrangian resolution (in terms of the number of triangular elements on the capsule surface denoted by N_L) is also shown in Fig. 6a by keeping the Eulerian resolution fixed at 120^3. Deformation decreases with increasing N_L. We note that D is significantly over-predicted for $N_L < 1280$. Above this N_L, D is nearly constant; as N_L is increased from 5120 to 20,480, D changes by only 0.4%.

The effects of varying timestep size (Δt) and computation box size (H_x) are shown in Fig. 6b for $Ca = 0.2$. D increases with decreasing Δt and increasing H_x, but reaches asymptotic values for $\Delta t \leqslant 10^{-3}$ and $H_x/a > 3$. As Δt is decreased from 0.01 to 0.001, D increases by 4.2%, but as Δt is decreased from 0.001 to 0.0001, D increases by only 0.8%. As H_x/a is increased from 0.5π to π, D increases by 5.1%, but as H_x/a is increased from π to 2π, D increases by only 1%. Results presented in Figs. 4–10, and in Tables 1–3 are for $H_x/a = \pi$.

Fig. 6 shows that at the best resolution ($N_E = 160^3$), our prediction for D ($= 0.5$) is the closest to, but still 4% less than, that obtained by Lac et al. (=0.52). This prediction is, however, better than that obtained by Li and Sarkar (=0.49).

In Table 2, we present the values of the inclination angle θ that the major axis of the capsule makes with the X-axis after it has reached a steady-state. The orientation angles obtained from our simulations also agree very well with those of RP and L1.

In Table 3, we present the period of the tank-treading motion (TTP) of the capsule, and compared that with the results of RP and L1. TTP is computed in two different ways: by following a full revolution of a marker point, and by integrating $\mathrm{d}l/|v|$ where $\mathrm{d}l$ is a line segment over the capsule profile in (x, y)-plane, and v is marker point velocity. As shown in Table 3, the former approach gives higher values of TTP. For $Ca \leqslant 0.15$, TTP computed using the second approach agrees well with those of L1 with maximum difference of 3% at $Ca = 0.025$. For $Ca = 0.2$, Lac et al. used the first approach, and their result agrees within 0.45% of ours.

At low Ca, neo-Hookean membrane tends to exhibit buckling (L1; Li and Sarkar). As shown by these authors, buckling onsets due to membrane zones undergoing compression in the equatorial region. In Fig. 7 we show the distribution of the elastic tension in the membrane for $Ca = 0.025$. Compressive (negative) stress in the equatorial region of the capsule is evident in the figure.

In Fig. 8, we show the effect of the viscosity ratio $\lambda = \mu_c/\mu_0$ on the steady state values of D, and compare our results with those of RP. This figure again shows that for $\lambda \neq 1$, as well, our results are in good agreement with those of RP.

The trajectory of a marker point on the capsule surface is shown in Fig. 9 and compared with the results of Lac et al. (2004). This result also shows excellent agreement between the two simulations.

3.2. Resolution test

Sensitivity of our results to the Eulerian and Lagrangian resolutions was shown earlier in Fig. 6 for $Ca = 0.2$. Further results for $Ca = 0.1$ are shown in Fig. 10 by considering three test simulations at different resolutions: (i) 80^3 Eulerian grids and 1280 Lagrangian

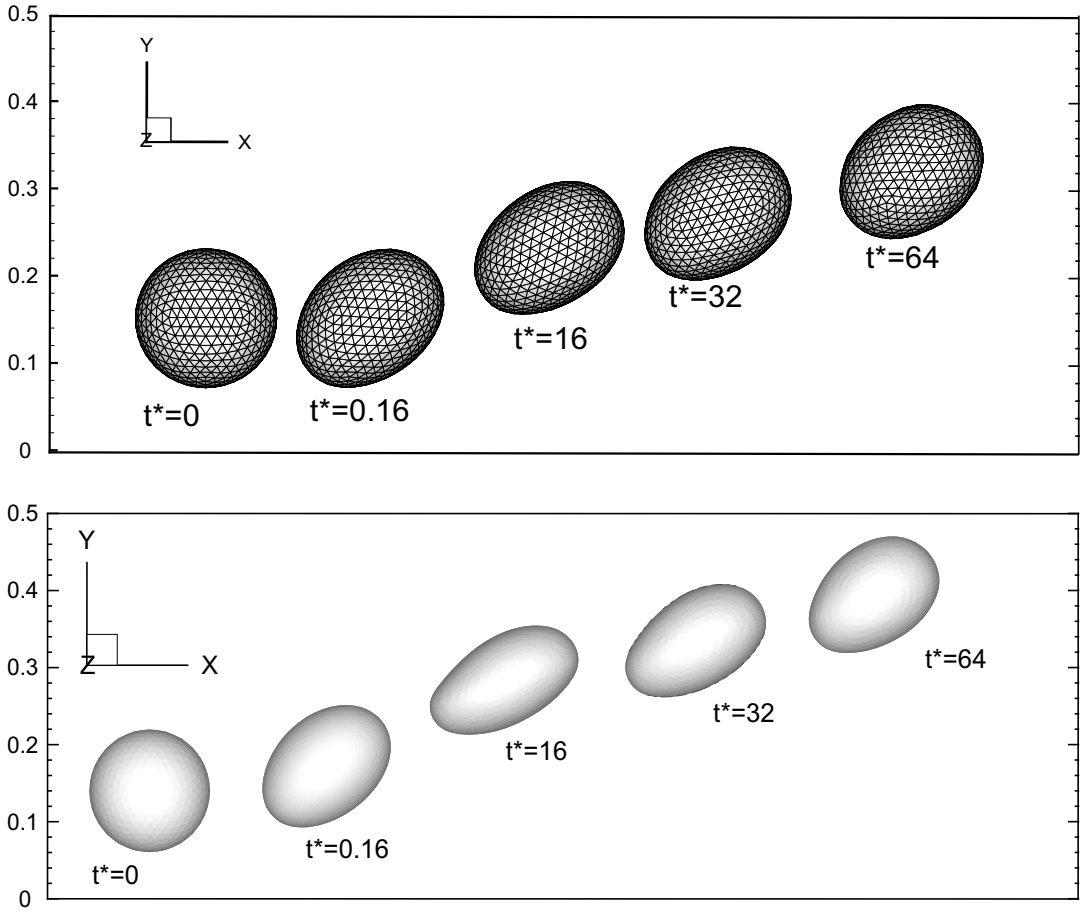

Fig. 12. Same as in Fig. 11, but over an extended period of time. $Ca = 0.2$ (top), and $Ca = 0.8$ (bottom).

elements; (ii) 120^3 Eulerian grids and 1280 Lagrangian elements; (iii) 120^3 Eulerian grids and 5120 Lagrangian elements. In Fig. 10b, we show the time history of D, and in Fig. 10b, we show the final steady shape in the shear plane. No significant difference is observed between the three test cases.

We also keep track of the capsule volume during the simulations. The change in the cell volume is less than ±0.1% from its initial volume. The projection method used here for the flow solver satisfies the mass conservation up to $\approx 10^{-14}$ at every grid point in the computational domain.

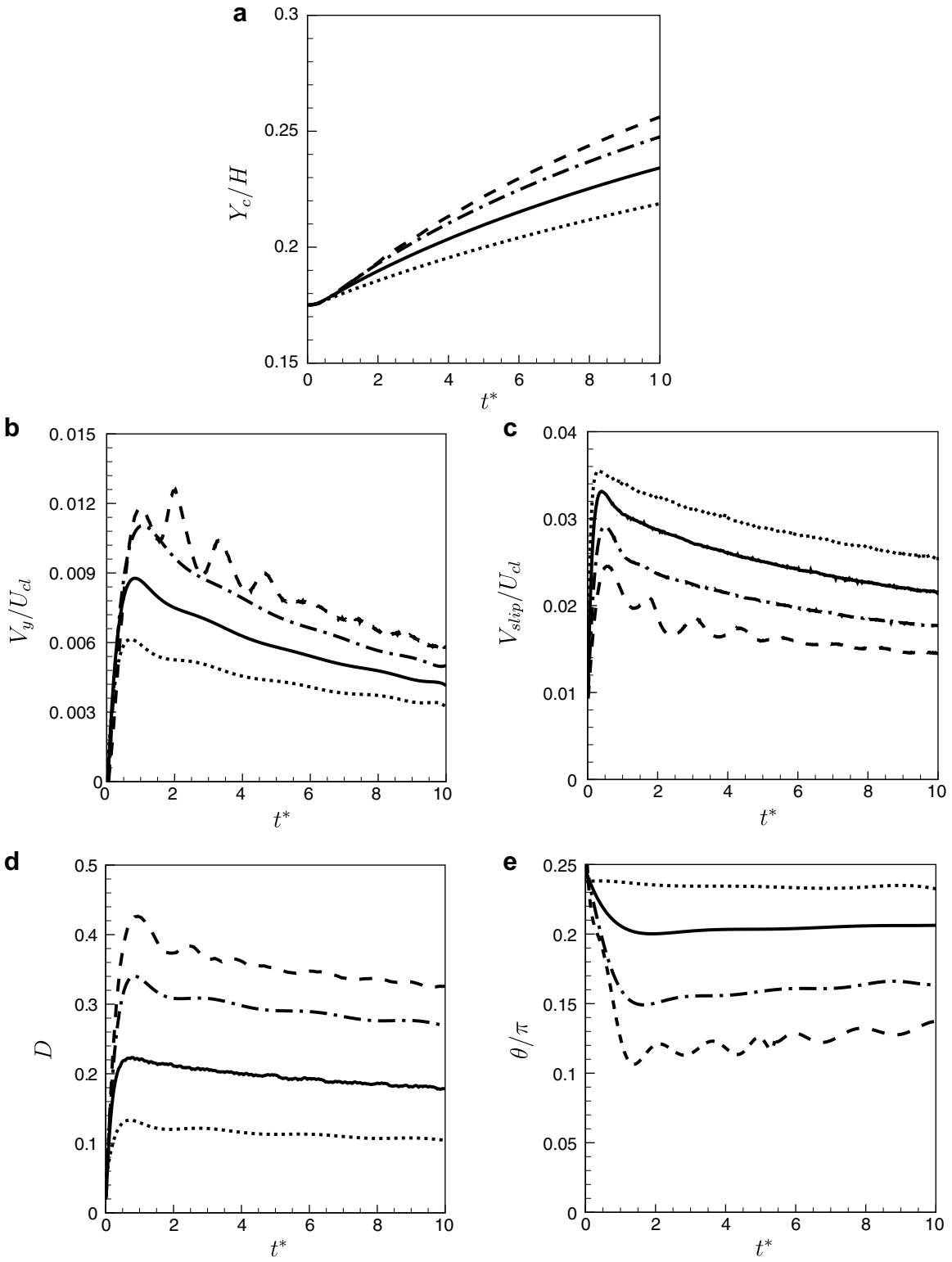

Fig. 13. History of (a) lateral distance, (b) lateral velocity, (c) slip velocity, (d) deformation, and (e) orientation (w.r.t. X-axis) of a capsule as a function of Ca. ····· $Ca = 0.1$; —— $Ca = 0.2$; –·–·– $Ca = 0.4$, and – – – $Ca = 0.8$. Here a/H=0.16, and $\lambda = 1$.

4. Results and discussion

4.1. Migration at $\lambda = 1$

We now consider the motion of a capsule in a fully-developed Poiseuille flow in a channel. As mentioned before, the imposed periodicity of the computational domain along the X and Z directions implies that we consider the motion of an array of capsules (Fig. 1), rather than a perfectly 'isolated' capsule. The inter-capsule distance is taken to be $L_{x0} = L_{z0} = H$. The effect of inter-capsule spacing will be considered in a later section.

We now consider the motion of a capsule in a fully-developed Poiseuille flow in a channel. As mentioned before, the imposed periodicity of the computational domain along the X and Z directions implies that we consider the motion of an array of capsules (Fig. 1), rather than a perfectly 'isolated' capsule. The inter-capsule distance is taken to be $L_{x0} = L_{z0} = H$. The effect of inter-capsule spacing will be considered in a later section.

The initial transience immediately after the capsule is released in the flow is shown in Fig. 11 for $Ca = 0.2$ and 0.8. For this case, we consider $a/H = 0.16$. We use 1280 and 5120 Lagrangian elements for $Ca = 0.2$ and 0.8, respectively. The capsule is released close to the wall at $Y_c/H = 0.175$ at $t^* = 0$. It deforms very quickly (within $t^* < 1$, as shown) under the action of the imposed shear, and aligns itself at an angle with the direction of the flow. For $Ca = 0.2$, the capsule attains an ellipsoidal shape, but for $Ca = 0.8$, the capsule shape at $t^* > 1$ is asymmetrical with high-curvature corner in the near-wall side. As expected, deformation and alignment w.r.t. the X-axis are higher for $Ca = 0.8$.

Migration of the capsule over an extended time ($tU_{cl}/a > 400$) until the capsule comes close to the center of the channel is shown in Fig. 12. For both Ca, the capsules migrate continually towards the centerline. Deformation decreases as the capsule moves closer towards the center in the low shear region. For $Ca = 0.8$, the shape is asymmetric when the capsule is located near the bottom wall, and near the channel center. Figs. 11 and 12 suggest that the rate of deformation is significant during the initial transience. Once this initial transience is passed, capsule shape remains nearly steady as it migrates away from the wall.

In Fig. 13 we show the history of lateral location, migration velocity V_y, slip velocity V_{slip}, deformation, and angular orientation w.r.t. X-axis for $Ca = 0.1$, 0.2, 0.4, and 0.8. For all cases, $a/H = 0.16$ and capsules are released at $Y_c/H = 0.175$. At high Ca, capsule shape is not ellipsoidal. In this case, D is calculated as $(L_{max} - L_\perp)/(L_{max} + L_\perp)$ where L_{max} is the maximum distance between two points on the capsule profile on (x, y)-plane, and $L_\perp$ is the distance between capsule membrane in the direction normal to L_{max} in the same plane. For an ellipsoidal capsule, L_{max} is the major axis, and $L_\perp$ is the minor axis. The orientation angle θ reported for non-ellipsoidal shape is the angle between L_{max} and x-axis. As the flow starts, D

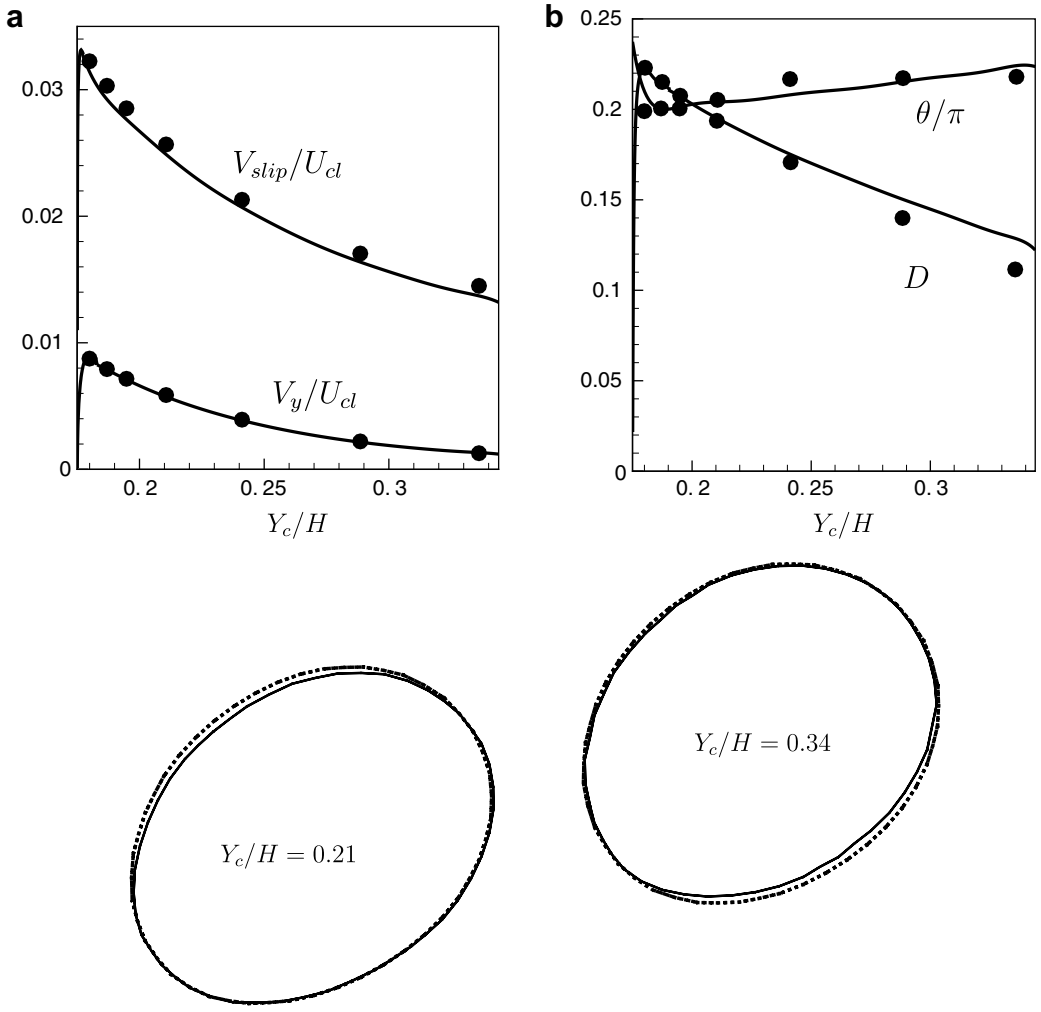

Fig. 14. Comparison of a free capsule with quasi-steady results for $Ca = 0.2$, $\lambda = 1$, and $a/H = 0.16$. In (a) and (b) lines are for the free capsule, and dots are for the quasi-steady results. Capsules shapes at two different locations are shown in the bottom. Solid line is the free capsule, and dash line is the quasi-steady result.

attains its peak value within a short time ($t^* < 1$) implying that the capsule deforms quickly before it moves significantly in the lateral direction. The migration velocity and slip velocity also reach their maximum, and the orientation angle reaches its minimum, during the rapid initial transience. The migration velocity and deformation are observed to be higher with increasing *Ca* implying that

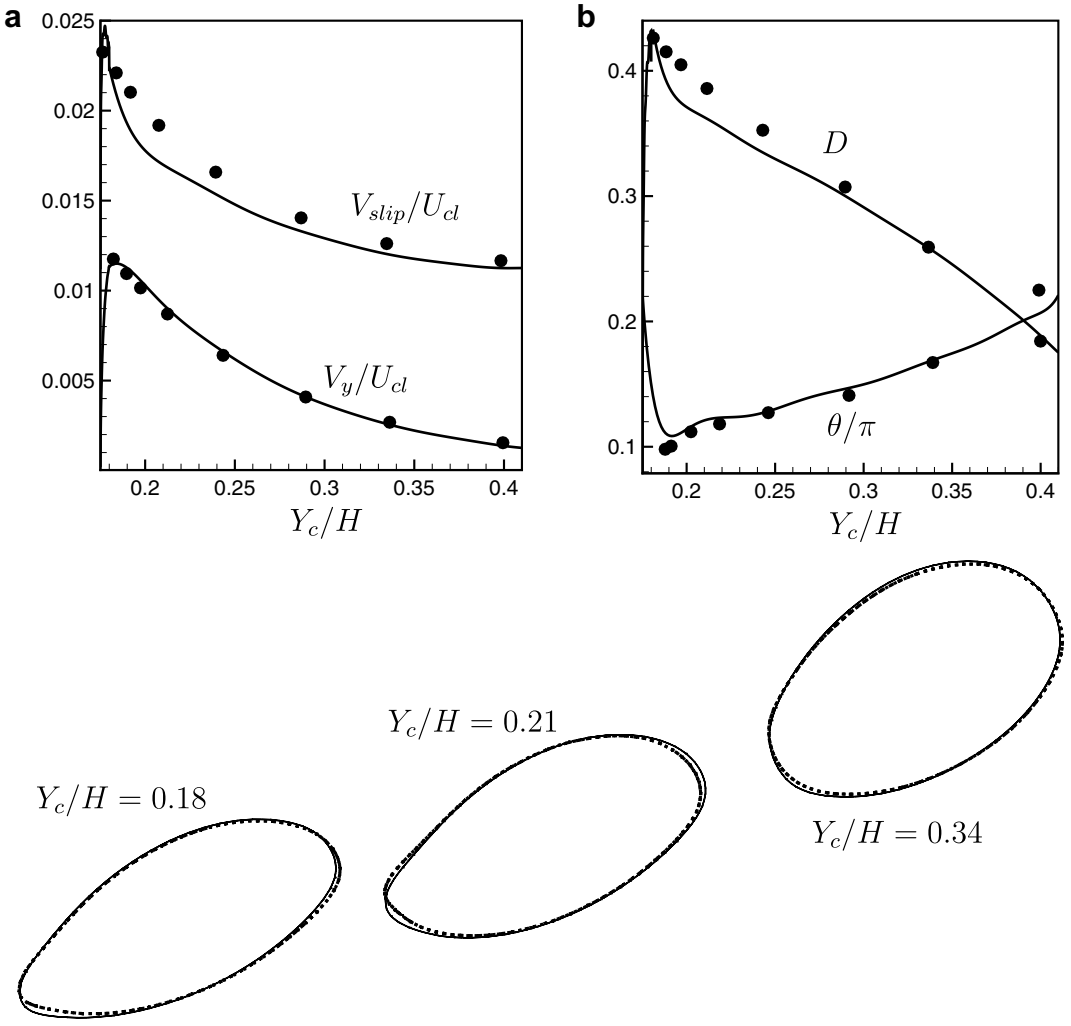

Fig. 15. Same as in Fig. 14, but for $Ca = 0.8$.

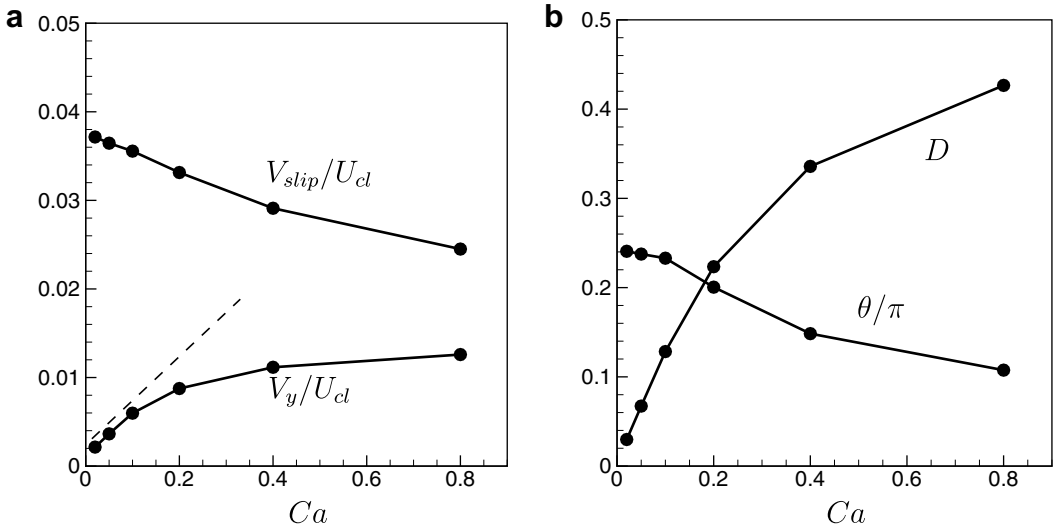

Fig. 16. Dependence of migration velocity, slip velocity, deformation, and orientation on *Ca* while keeping a/H and Y_c/H constants at 0.16, and 0.18, respectively.

the lateral migration is essentially due to the departure from the initially undeformed spherical shape as in case of a liquid drop. The angular orientation w.r.t. the *X*-axis decreases with increasing *Ca*, which is also consistent with the results in linear shear flow, and seem to remain the same even in presence of the wall-bounded parabolic flow. The slip velocity V_{slip}, defined as the Poiseuille velocity at the instantaneous center of the capsule minus the *X*-component of the capsule velocity, is shown in Fig. 11c. The slip velocity is always positive meaning that the capsule lags behind the fluid. The slip velocity becomes higher with decreasing *Ca*. The slip velocity is order of magnitude less than the capsule translational velocity. In the limit $Ca \to \infty$, the slip velocity would vanish, whereas in the limit that the capsule is perfectly rigid, it would be maximum for a given lateral location. This qualitative trend is reflected in the simulation results. Once the initial transience is passed, the capsules start migrating toward the channel center. During subsequent motion, the deformation, migration and slip velocity decrease, and the orientation increases with time as the capsule drifts toward low shear region. The decrease in slip velocity over time (i.e. with lateral location) is also in qualitative agreement with the asymptotic theory of small rigid spheres as well as neutrally buoyant drops at small deformation. The capsule migrates toward the center of the channel for all values of *Ca* considered here. The migration in general is slow. For $Ca = 0.8$ the capsule travels only about half of its diameter in the lateral direction, while translating nearly 50 diameters along the axial direction.

Fig. 13 shows oscillations in V_y, V_{slip}, D, and θ for $Ca = 0.8$. The oscillations arise from the shape oscillation of the capsule which can be seen from capsule profiles given in Fig. 11. This figure shows that immediately after the release ($t^* = 0.16$ and 0.64), capsule shape is ellipsoidal. But for $t^* \geqslant 0.96$, sharp edge is developed near the wall-ward side due to the higher local shear stress acting on this region of the capsule arising from the no-slip condition imposed on the wall. Because of the tank-treading, the sharp curvature travels along the membrane, and it dissipates as it moves away from the wall ($t^* = 2.4$). Subsequently, another sharp curvature develops near the wallward region ($t^* = 3.3$ and 4.1), which also travels along the membrane away from the wall. As the capsule migrates away from the wall, the sharp curvature weakens. Due to repeated emergence and smoothening of the sharp curvature, magnitude and direction of L_{max} and $L_\perp$ oscillate, causing an oscillation in D and θ. Oscillations in V_y and V_{slip} also arise due to shape oscillation. V_y is locally minimum when the curvature is high, and maximum when it is smoothened. The oscillations are not evident beyond $t^* = 5$ over which the capsule travels only 0.28 of its diameter. Thus, these oscillations are during initial transience. Since migration is a slow

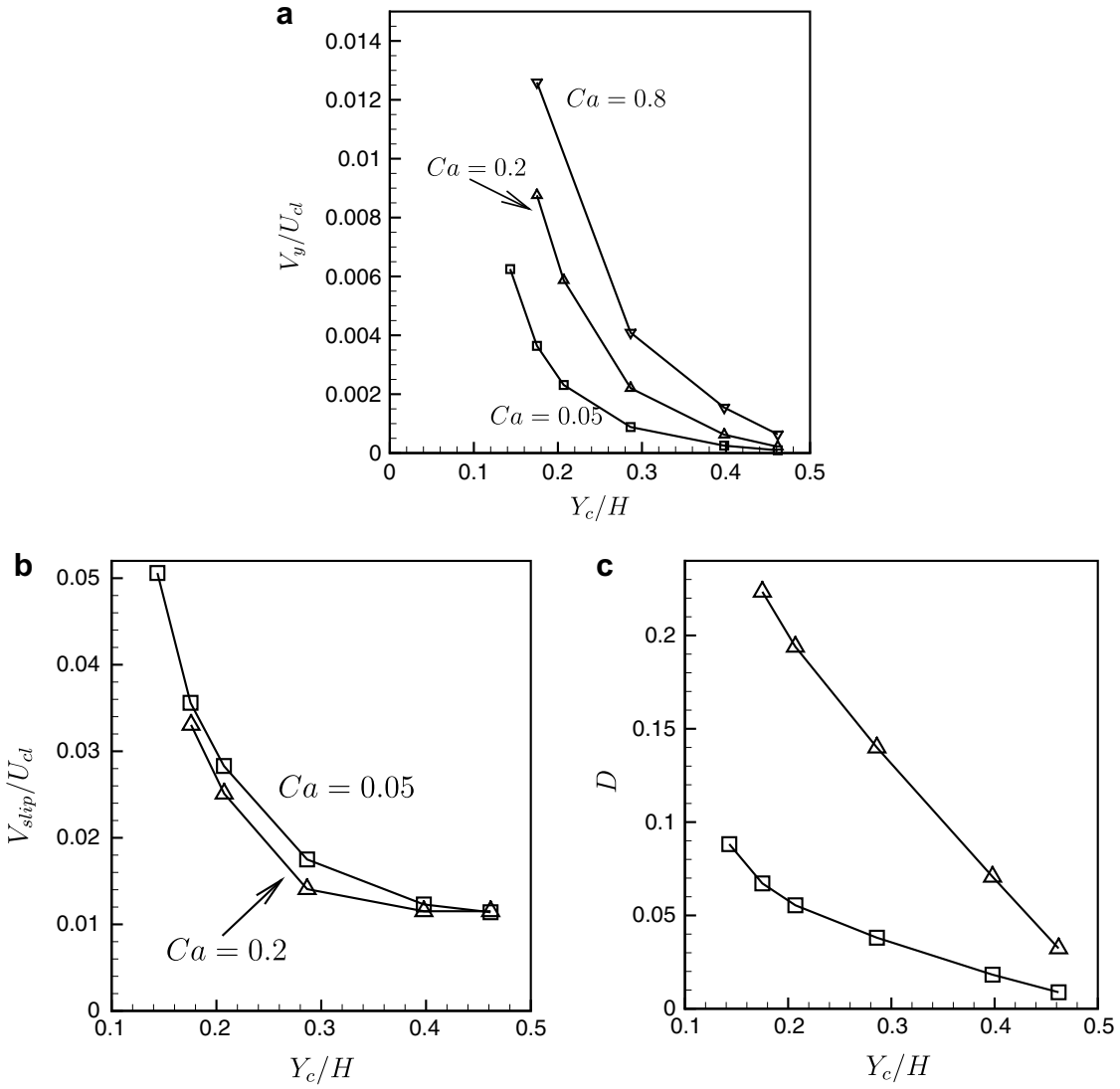

Fig. 17. (a) Variation of V_y, (b) V_{slip}, and (c) D w.r.t. Y_c while keeping Ca and $a/H = 0.16$ fixed.

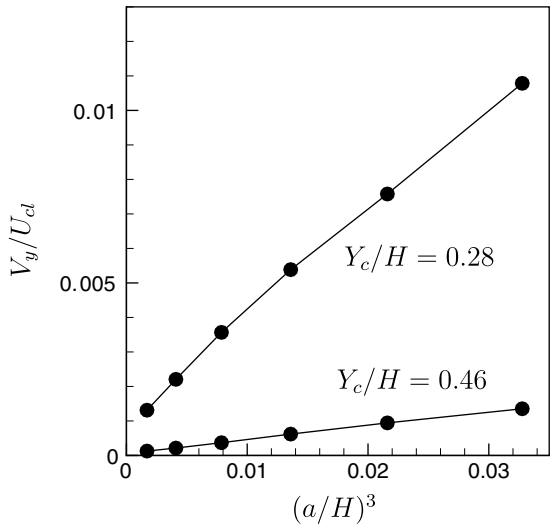

Fig. 18. Variation of V_y w.r.t. a/H at constant Ca and Y_c/H. Ca is fixed at 0.2.

process, and as shown in Fig. 12, the capsule does not reach the center even at $t^* = 64$, these oscillations do not have any effect on the long-term migration.

It is of interest to see if the motion of the capsule, after the initial transience is passed, is quasi-steady. We compare the motion of a 'free' capsule with the results of a 'quasi-steady' simulation in Figs. 14 and 15 for $Ca = 0.2$ and 0.8, respectively. For the simulation of a free capsule, the capsule is released near the bottom wall and the simulation is continued until it reaches close to the center. For the quasi-steady simulations, an undeformed spherical capsule is released at various lateral locations along the trajectory of the free capsule, and the simulations are stopped just after the initial transience is passed. Since the capsule has not moved significantly in the lateral direction during this short simulation, the results, such as migration velocity, deformation, etc., can be taken as the 'quasi-steady' results corresponding to that lateral location. In Figs. 14 and 15, we compare four quantities: migration velocity, slip velocity, deformation, and angular orientation, of the free capsule and quasi-steady result. In the figure the lines represent the free capsule, and the points represent quasi-steady results. As can be seen for both $Ca = 0.2$ and 0.8, all four quantities show excellent agreement between the free capsule and the quasi-steady results. Note that in the limit the capsule is located at the center of the channel, the slip velocity is still non-zero and proportional to $(a/H)^2$ according to the linear theory. The asymptotic behavior of computed V_{slip} in Fig. 13a yields the same order of magnitude value as $(a/H)^2$.

In Figs. 14 and 15, we also overlap the shapes of the freely moving capsule and the quasi-steady results for various lateral locations. The capsule shapes match very well which further confirms that the migration is a quasi-steady process.

The quasi-steady nature of the capsule migration can be understood by comparing the migration time $T_y = a/V_y$, to the response time of the capsule shape $T_c = \mu a/Eh$. The capillary number $Ca = \mu U_{cl}/Eh$ can be expressed as the ratio of T_c and the axial convection time $T_x = a/V_x$, where $V_x \approx U_{cl}$. Since $V_y \ll V_x$ (that is, $T_x/T_y \ll 1$), and $Ca < 1$, we see that $T_c \ll T_y$.

It is also of interest to compare the present results with previous analytical predictions. Migration of a capsule with Hookean membrane was considered by Helmy and Barthes-Biesel (1982) in an unbounded cylindrical Poiseuille flow in the limit of $Ca(a/D_0) \ll 1$, where D_0 is a length scale of the undisturbed flow, which is the tube diameter for the Poiseuille flow. They predicted

$$\frac{V_y}{U_{cl}} = -\frac{29}{6} Ca \left(\frac{b}{a}\right)\left(\frac{a}{D_0}\right)^3 \tag{23}$$

for Poisson ratio equal to 1/2 for the membrane. Here b is the distance of the capsule center from the flow centerline.

Chan and Leal (1979) considered migration of a deformable liquid drop of surface tension σ in an unbounded plane Poiseuille flow in the limit of small deformation, and obtained

$$\frac{V_y}{U_{cl}} = -\frac{8}{5}\frac{\mu_0 U_{cl}}{\sigma}\left[1 - 2\left(\frac{Y_c}{H}\right)\right]\left(\frac{a}{H}\right)^3 \tag{24}$$

for $\lambda = 1$. Despite the differences in the background flow, and the nature of the particle, (23) and (24) predict the similar qualitative dependence of V_y/U_{cl} on $Ca, Y_c/H$ and a/H, and differ only in the numerical prefactors. Though exact comparison is not possible due to the differences in the background flow and the nature of the particle, it is of interest to see if the qualitative dependence of V_y/U_{cl} w.r.t. $Ca, Y_c/H$ and a/H predicted by (23) and (24) agree with our simulation.

In Fig. 16a we show the migration velocity as a function of Ca while keeping a/H and Y_c/H constants at 0.16 and 0.18, respectively. The capsules were released at $Y_c/H = 0.175$, and hence the

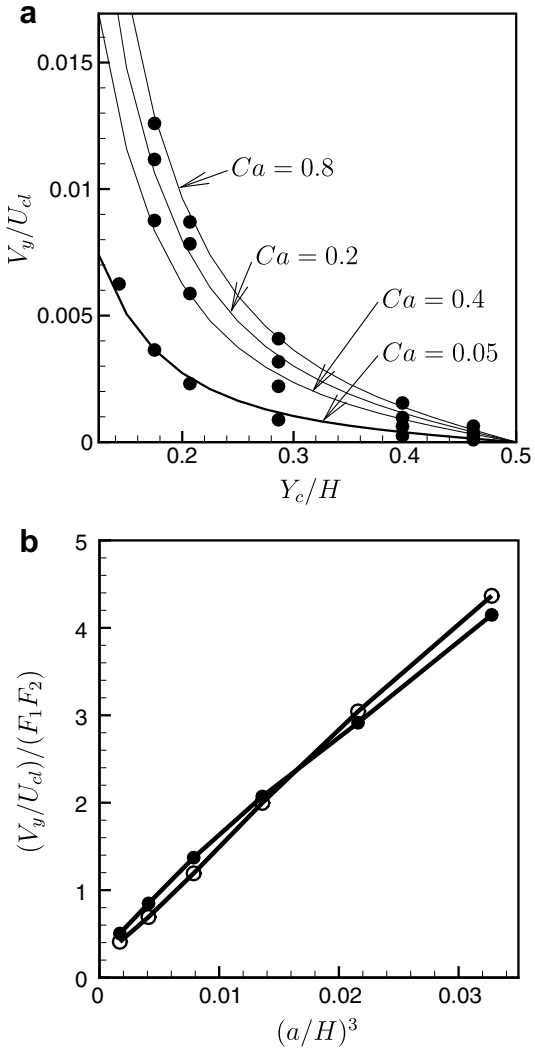

Fig. 19. (a) Comparison of the scaled shape function C_s (solid line), and the numerical migration velocity (filled circles) for $a/H = 0.16$. (b) Replotting Fig. 16 by scaling V_y by (F_1F_2).

wall effect is strong. While (23) and (24) predict a linear dependence of V_y on Ca, the simulations predict a non-linear dependence. The results in Fig. 16 are shown for $0.025 \leqslant Ca \leqslant 0.8$. Assuming that the linear dependence of V_y on Ca is valid at low Ca (which is likely to be the case), and extrapolating the result to higher Ca (dash line in Fig. 16a), we see that the linear theory over-predicts the migration velocity at higher Ca. This is because the linear theory over-predicts also the capsule deformation at higher Ca (Table 1).

We also show slip velocity, deformation, and orientation as functions of Ca in Fig. 16. Fig. 16a shows that the slip velocity decreases with increasing Ca. For a small, rigid sphere in a circular Poiseuille flow, the ratio $V_{slip}/U_{cl} = b^2/(D_0/2)^2 - (2/3)(a/D_0)^2$, to the leading order (Brenner, 1970; Goldman et al., 1967) where b and D_0 are defined above. In the linear theory of Helmy and Barthes-Biesel (1982), the axial velocity of the capsule does not depend on Ca, and the ratio V_{slip}/U_{cl} is the same as that of a small rigid sphere. Our simulations show that V_{slip}/U_{cl} depends on Ca. Further, the order of magnitude of V_{slip}/U_{cl} obtained from the simulation and shown in Fig. 16a is significantly lower than the prediction by the linear theory even when $Ca = 0.025$ is considered. On the contrary, the simulation and the linear theory would predict nearly similar order of V_{slip} as $b \to 0$, that is when the capsule is located far from the wall as observed in Fig. 15a. Shapira and Haber (1990), on the contrary, obtained that V_{slip}/U_{cl} is proportional to $Ca(a/Y_c)^2$, for a wall-bounded linear shear flow in the limit of small deformation. Assuming that the linear dependence of V_{slip} on Ca is valid at low Ca even for parabolic flow, and extrapolating the result to higher Ca, one can say from Fig. 16a that the linear theory, when taken into consideration the effect of Ca, would underpredict the slip velocity at higher Ca.

In Fig. 16b, deformation D and orientation angles are shown. D appears to approach a plateau as Ca increases which explains the plateau in migration velocity. This plateau in D can arise from two effects. In an unbounded linear shear flow, D does not increase linearly at large Ca, and shows reduced rate of change at higher Ca. In addition, the presence of the wall and parabolic nature of the flow can further prevent the capsule from deforming at higher Ca. In an wall-bounded flow, migration arises from two effects. A particle moving near a wall would experience a lift force even in absence of the flow due to the asymmetry introduced by the wall. In addition the presence of a shear flow would introduce additional asymmetry in the governing equations at low inertia leading to the deformation-induced lift force. Thus the migration velocity is proportional to the product of slip velocity and amount of deformation. This explains, as seen in Fig. 16, that D increases but V_{slip} decreases with increasing Ca resulting a plateau in V_y at higher Ca.

In Fig. 16b, the orientation angle at very low Ca is close to its theoretical value of $\pi/4$ for low deformation. It decreases with increasing Ca departing from the linear theory, but appears to plateau at higher Ca due in part, possibly, to the wall effect.

In Fig. 17 we plot V_y, V_{slip}, and D as functions of Y_c/H while keeping Ca and a/H fixed. Unlike the linear dependence in (23) and (24), the simulations predict non-linear dependence of V_y w.r.t. Y_c/H.

In Fig. 17b, variation of V_{slip} w.r.t Y_c/H shows also a non-linear decrease. The slip velocity is higher near the wall and decreases

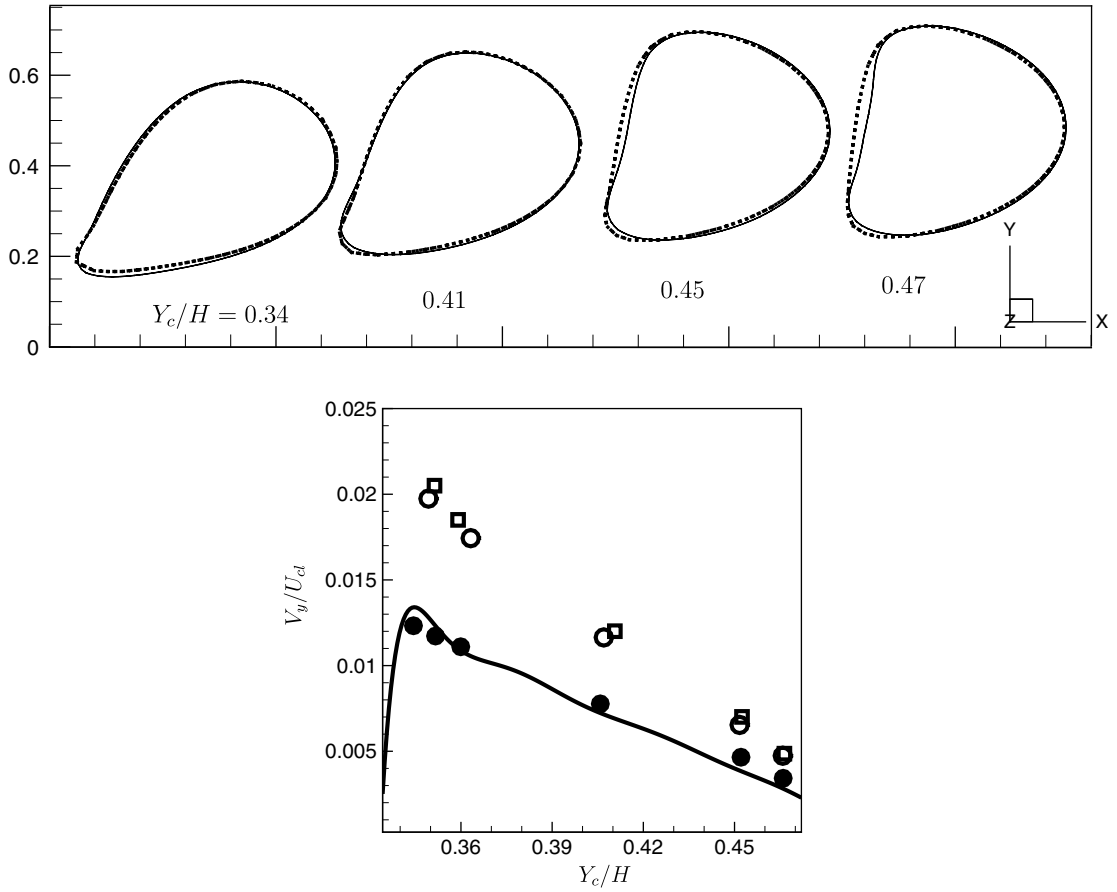

Fig. 20. Migration of a capsule at $a/H = 0.5$, and $Ca = 0.2$. Top: deformed shapes for free capsule (solid line), and quasi-steady simulations (dash line). Bottom: lateral velocity for free capsule (solid line) and quasi-steady results (filled circles). Also shown is the effect of increasing separation distance between consecutive capsules: filled circles, open circles and boxes correspond to $L_{x0}/a = 2, 6$ and 8, respectively.

away from the wall. The higher slip velocity near the wall arises from the no-slip condition imposed on the wall which causes a higher local shear rate in the gap between the capsule and the wall. When wall-effect is included (Chan and Leal, 1979; Chaffey et al., 1967; Magnaudet, 2003), V_{slip} should decrease as $(1 - Y_c/(H/2))^2$, in the leading order for small rigid spheres as well as neutrally buoyant drops under small deformation. Our numerical results indicate that V_{slip} decreases faster than this rate near the wall, and slower near the centerline. D shown in Fig. 17c also suggests a faster decrease near the wall than that near the centerline.

In Fig. 18 we plot V_y as a function of $(a/H)^3$ while keeping Ca and Y_c/H constants. Interestingly, the linear dependence of V_y w.r.t. $(a/H)^3$ as predicted by (23) and (24) happens to be the case in the numerical results as well.

Shapira and Haber (1988) studied the wall effect on the shape of a drop moving in a quiescent fluid confined between two parallel plates in the limit $a/H \ll 1$, and predicted

$$D = \frac{175}{384}\frac{\mu V_x}{\sigma}\left(\frac{a}{H}\right)^2 C_s \tag{25}$$

where C_s is a function of Y_c/H which is maximum at the channel wall, and zero at the center, implying that drop deformation decreases as it is located closer to the center, and that deformation is zero at the center as is the case for small a/H. Though Shapira and Haber (1988) considered a non-migrating drop with a constant orientation at $\pi/4$, we find that the expression of C_s can be used to predict the dependence of V_y on Y_c. This is shown in Fig. 19a where data points are numerical V_y at various Y_c locations, and solid lines are the shape function C_s scaled by a factor for each Ca.

The results shown in Fig. 19a are for a fixed $a/H = 0.16$, the lowest size ratio considered. Since the numerical results agree with the theoretical prediction (23) and (24) on the linear dependence of V_y on a/H, the scaling factor used for C_s should depend only on Ca. Based on the numerical results in Figs. 18 and 19a, and following the theoretical results of Shapira and Haber (1988), an approximate expression for the migration velocity can be proposed as

$$\frac{V_y}{U_{cl}} = F_1(Ca)F_2(Y_c/H)\left(\frac{a}{H}\right)^3, \tag{26}$$

where the functions F_1 and F_2 are functions of Ca and Y_c/H, respectively, and are given as

$$F_1 = \exp[-0.3458\ln(Ca) + 7.3878] \tag{27}$$

and

$$F_2 = \exp\left[-11.1758\left(\frac{Y_c}{H}\right) - 2.7429\right]. \tag{28}$$

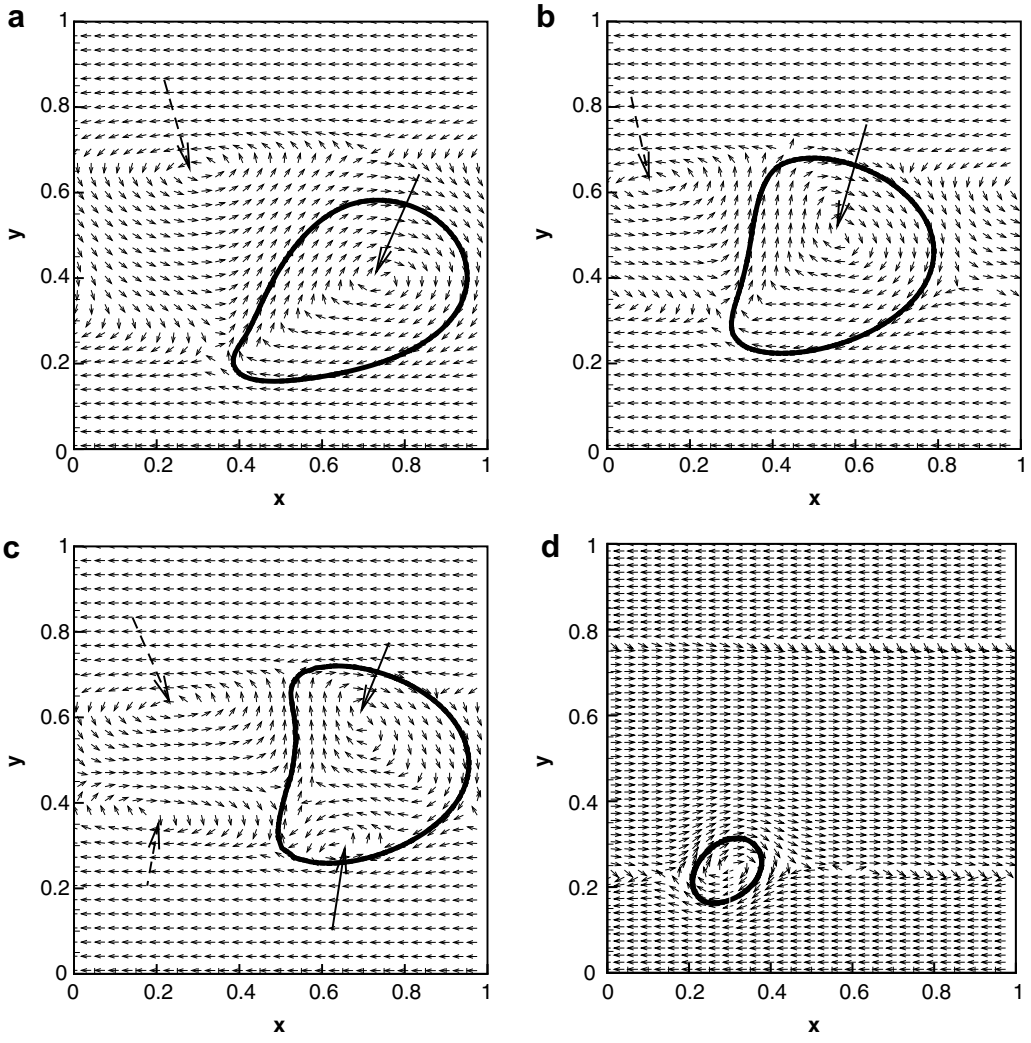

Fig. 21. Velocity vectors drawn in the XY plane passing through, and in a frame of reference moving with, the capsule center of mass. (a)–(c) are for $a/H = 0.5, Ca = 0.2$ at $Y_c/H = 0.35$, 0.44, and 0.46, respectively. (d) for $a/H = 0.16$.

F_2 is a simplified form of the original shape function C_s given by Shapira and Haber. In Fig. 19b, we replot the migration velocity shown in Fig. 18 (which was for a constant $Ca = 0.2$ but different Y_c/H) by scaling V_y/U_{cl} by (F_1F_2). We find that curves for different Y_c/H collapse, and vary linearly with $(a/H)^3$. Eqs. (26)–(28) can thus be used to reasonably predict migration rate of a capsule in a parabolic flow in a channel for moderate values of (a/H) and Ca.

4.2. Larger capsules

We consider $a/H = 0.5$ for which we use 5120 Lagrangian elements on the capsule surface. The computational domain is cubic, and the distance between the adjacent capsule centers in the array is $L_{x0} = L_{z0} = H$. The capsule is released at $Y_c/H = 0.334$. Fig. 20 shows the deformed shapes at various lateral locations for $Ca = 0.2$. Unlike the smaller capsules which attain ellipsoidal shape after the initial transience is passed, the initial shape (at $Y_c/H = 0.34$ in Fig. 20) for $a/H = 0.5$ resembles a tear-drop and is asymmetric with the high-curvature end facing the bottom wall. Center-ward migration is evident in the figure. As the capsule approaches the center, it changes from a tear-drop to a slipper shape. In the figure, we also overlap the quasi-steady shapes with those of the free capsules, and see that even for the larger capsule, the two simulations predict similar shapes. The migration velocity for the free capsule and the quasi-steady values are presented in Fig. 20 which also shows that the quasi-steady values match well with the results of the free capsules once the initial transience is passed.

Fig. 21 shows the fluid velocity vectors at three time instances during the migration of the larger capsule. The figures here are drawn in a reference frame moving with the velocity of the center

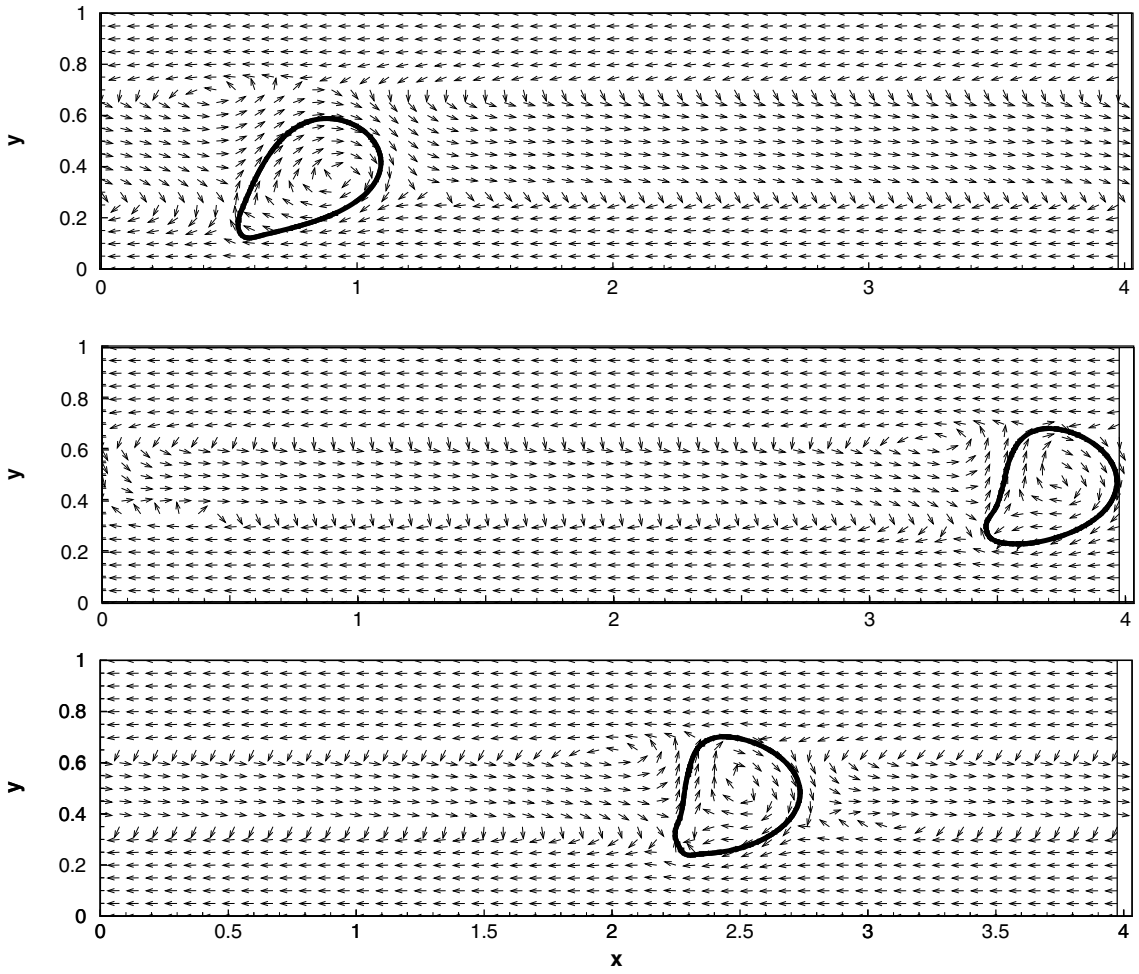

Fig. 22. Effect of separation distance on flow pattern: velocity vectors (in a frame of reference moving with the velocity of the capsule center of mass) corresponding to the case shown in Fig. 21a–c but for $L_{x0}/a = 8$.

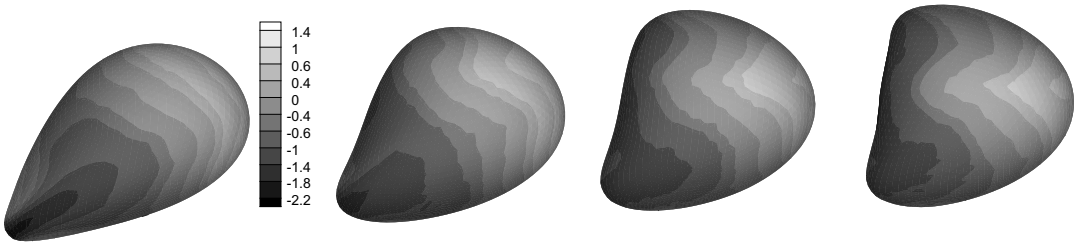

Fig. 23. Membrane stress distribution for the migrating capsule shown in Fig. 20. Dark regions correspond to compressive stress.

of mass of the capsule. Also shown is the vector plot for $a/H = 0.16$ at one time instance. During the initial phase of migration of the larger capsule, a clockwise rotating vortex is generated inside the capsule. The center of this vortex is located close to the capsule centroid. Due to the proximity of the larger capsules in the array, $(a/L_{x0} = 0.5)$, the fluid in between the adjacent capsules also develops a counter rotating vortex (marked by dash arrow in the figure). In case of smaller capsules, such vortex exterior of the capsule is absent. As the larger capsule approaches the center of the channel, the interior vortex moves upward, while a new smaller counter rotating vortex is generated near the bottom. In the exterior fluid as well, two counter rotating vortices can be seen, which are not present for the smaller capsule. The presence of exterior vortices for large a/H, and the transition from one vortex to two counter-rotating vortices as shown by our extended simulations, can have implications in case of tracer diffusion in capillary blood vessels in presence of erythrocytes. It should be mentioned that the strength of the internal vortex is actually very weak.

For larger capsules of $a/H = 0.5$, the effect of separation distance between consecutive capsules is shown in Fig. 20. We consider $L_{x0}/a = 2, 6$ and 8. The separation distance does have a significant effect on migration velocity when the capsule is located closer to the wall. As L_{x0}/a is changed from 2 to 6, V_y increases by a factor of 1.5; when L_{x0}/a is changed from 6 to 8, V_y increases by a

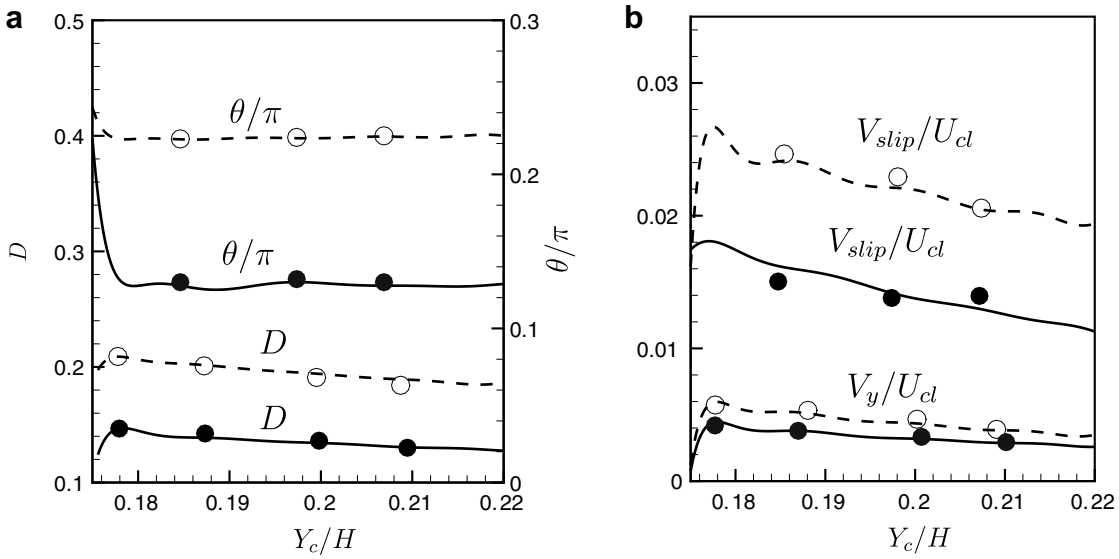

Fig. 24. Free capsule versus quasi-steady results for $\lambda \neq 1$. Lines represent free capsule and symbols represent quasi-steady simulations. Solid lines and filled circles represent $\lambda = 5$, dash lines and open circles represent $\lambda = 0.2$. $a/H = 0.16, Ca = 0.2$.

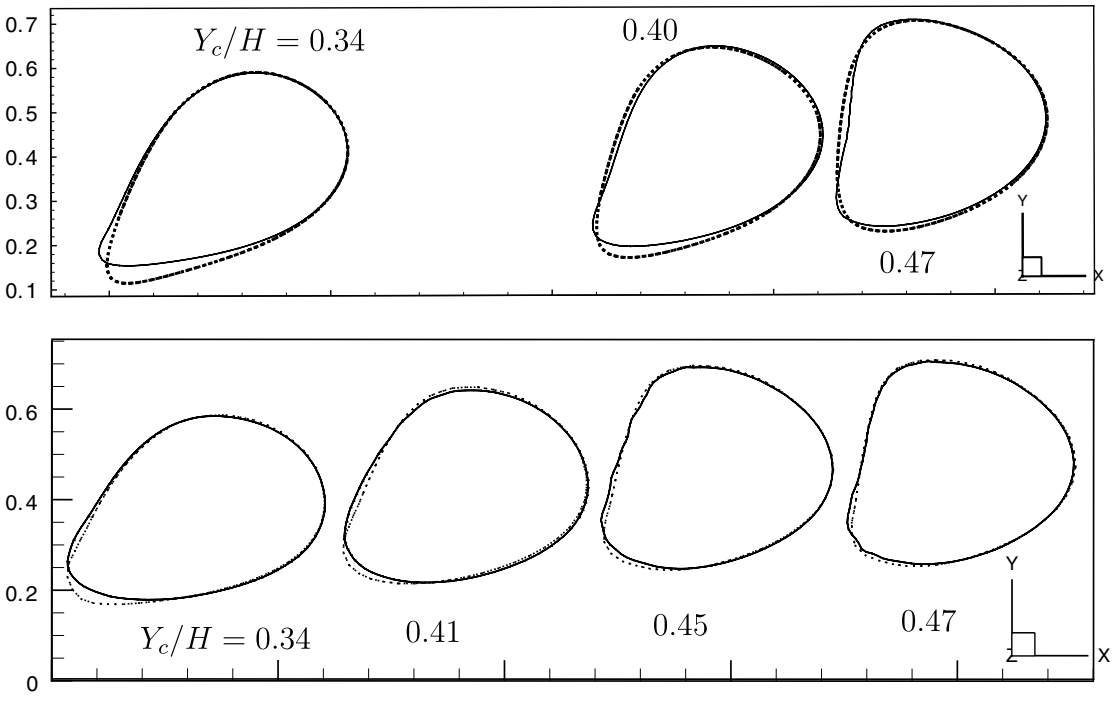

Fig. 25. Deformed shapes for $a/H = 0.5, Ca = 0.2$ at $\lambda = 0.2$ (top) and $\lambda = 5$ (bottom). Solid line is the free capsule, and dotted line is the quasi-steady result.

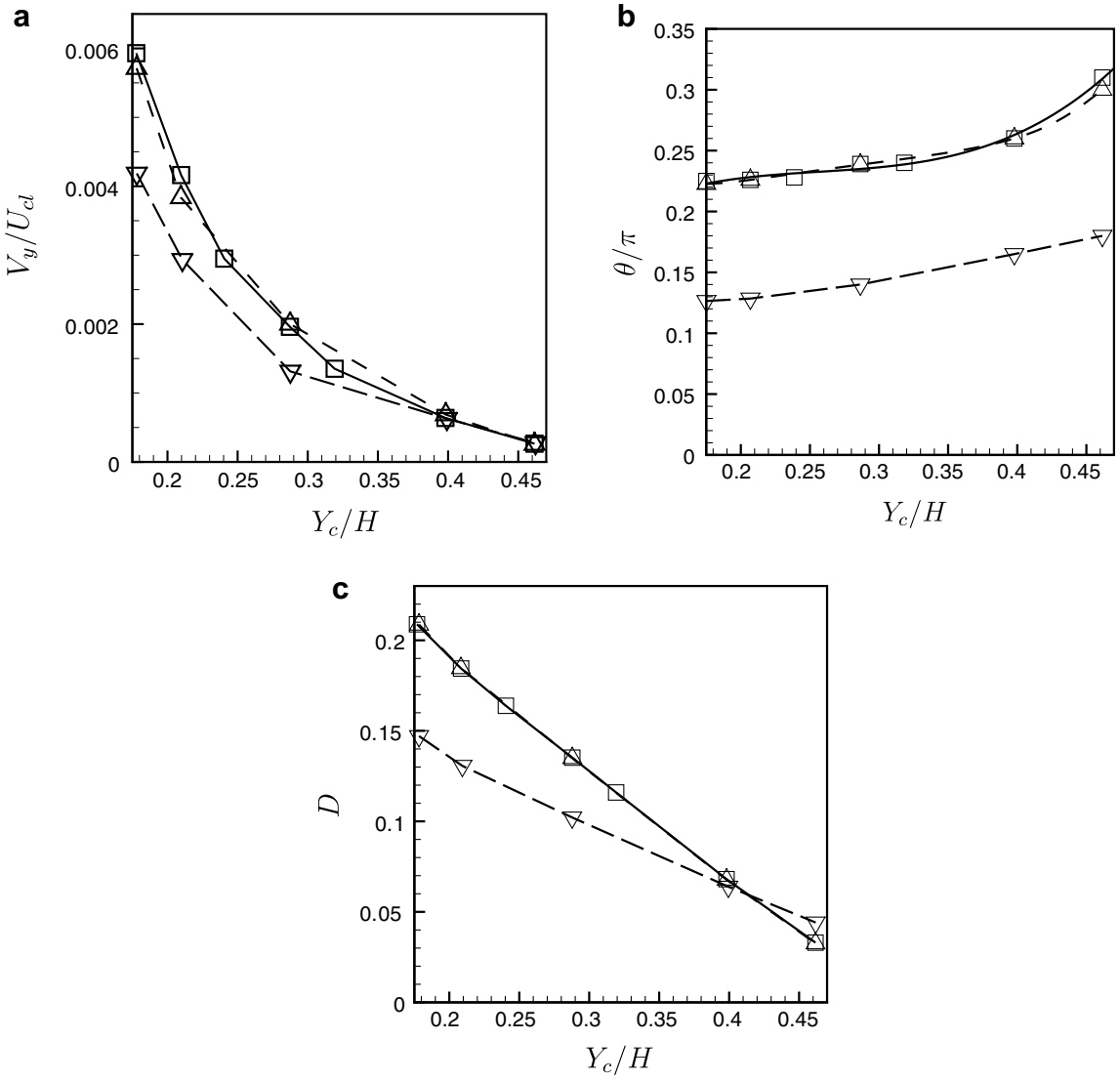

Fig. 26. Migration velocity, deformation, and orientation as functions of Y_c. $a/H = 0.16, Ca = 0.2$. □ $\lambda = 1$, △ $\lambda = 0.2$, ∇ $\lambda = 5$.

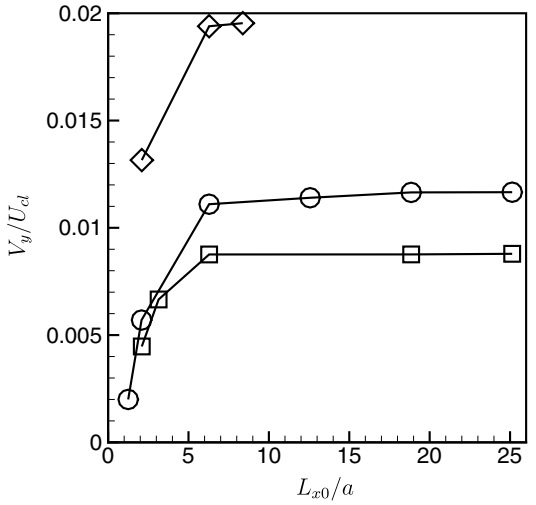

Fig. 27. Effect of separation distance L_{x0}. □ $Ca = 0.2$, $a/H = 0.16$; ∘ $Ca = 0.4$, $a/H = 0.16$; ∇ $Ca = 0.2, a/H = 0.5$. Migration velocities shown here correspond to the quasi-steady simulations.

factor of 1.05. Thus V_y is expected to converge with increasing L_{x0}/a. For this case, we have not performed a simulation with even higher L_{x0}/a due to computational cost, as $L_{x0}/a = 8$ itself was simulated using $320 \times 80 \times 80$ resolution. The effect of L_{x0} appears to decrease as the capsule moves away from the wall. Further result on the effect of L_{x0}/a on V_y for $a/H = 0.16$ is given later in Fig. 27 where convergence of V_y with increasing L_{x0}/a is evident. The flow pattern for $L_{x0}/a = 8$ is shown in Fig. 22 which can be compared with the results for $L_{x0}/a = 2$ shown in Fig. 21. Evolution of the internal and external vortices as the capsule migrates away from the wall is qualitatively similar for $L_{x0}/a = 8$ and 2.

For larger capsules shown in Fig. 20, the back of the membrane undergoes compression. This is shown in Fig. 23 where we plot the principal stress. Regions having negative stress are seen in this figure.

4.3. Effect of λ

Effect of λ is considered next by two simulations at $\lambda = 5$ and 0.2 (both for $a/H = 0.16$) shown in Fig. 24. Deformation, orientation, migration and slip velocity of a free capsule released at $Y_c/H =$

0.175 at $t^* = 0$ are shown. Also shown are the results from quasi-steady simulations of undeformed spherical capsules released at various lateral locations. The results from the free-capsule simulation and those of quasi-steady simulations agree well implying that the quasi-steady nature of migration is valid over the range of viscosity ratio considered here.

The capsule shapes for free capsule and for quasi-steady results are compared in Fig. 25 for $a/H = 0.5$, and $\lambda = 5$ and 0.2 at various lateral locations. The two simulations predict nearly overlapping shapes implying the quasi-steady nature of migration even for larger capsules at a viscosity ratio other than unity.

The migration velocity, deformation and orientation of the capsules for $\lambda = 5, 0.2$ and 1 over a wider range of lateral locations are shown in Fig. 26 for $a/H = 0.16, Ca = 0.2$. As expected, the migration rate, deformation and orientation angle decrease with increasing λ. The migration velocity and deformation decrease as the capsule approach channel center. We also note that results for $\lambda = 1$ and 0.2 nearly overlap with each other, which is consistent with the linear shear results presented earlier in Fig. 8 which showed that deformation did not change much from that of $\lambda = 1$ when λ is reduced below unity, but it changed significantly when $\lambda > 1$. Also note in Fig. 26 that near the center of the channel, the deformation curves for $\lambda = 1$ and $\lambda = 5$ cross each other. This is likely because a capsule with higher λ is slower to respond to the changing shear rate than the one with lower λ. The characteristic time for deformation is proportional to $1 + \lambda$. This also explains why migration velocities are nearly the same for $\lambda = 1$ and $\lambda < 1$, but much lower for $\lambda > 1$.

It may be noted that the expression of drop migration by Chan and Leal suggests that for $\lambda < 0.5$ and $\lambda > 10$, the drop migrates toward the center of a channel, while for $0.5 < \lambda < 10$, it migrates toward the wall. The simulations performed here over a range of Ca and λ suggested that the capsule migrates always toward the center of the channel.

4.4. Effect of capsule separation

The effect of separation distance on the migration velocity and flow pattern for $a/H = 0.5$ was shown earlier in Figs. 20 and 22. Further results for $a/H = 0.16$ at $Ca = 0.2$ and 0.4, and $a/H = 0.5$ at $Ca = 0.2$ are shown in Fig. 27. Here the dimensionless separation distance L_{x0}/a is varied from 1.25 to 25. As discussed earlier, migration velocity changes significantly for small separation distance, but converges beyond $L_{x0}/a \approx 6$. The migration velocity decreases as $-1/r$ where r is the separation distance. Comparison of V_y at four L_{x0}/H suggests that the results presented in the previous sections would change very little by increasing the separation distance, but they would change significantly with decreasing separation distance.

5. Conclusion

We present three-dimensional numerical simulations using front-tracking method on the motion of an array of liquid capsules enclosed by neo-Hookean membrane in a wall-bounded plane Poiseuille. In the context of physiological flows, the range of capsule size considered here is relevant for the motion of red blood cells through arterioles and venules. Extensive validation of the methodology is presented on capsule deformation in linear shear flow. The results, such as history and steady-state values of deformation parameter, orientation, tank-treading frequency, and trajectory of material points on the capsule surface, showed very good agreement in comparison to the boundary integral simulation of Lac et al. (2004), and Ramanujan and Pozrikidis (1998).

We then present results on the lateral migration of a capsule in a plane Poiseuille flow simulated over extended period of time. The migration is observed to be a quasi-steady process, except an initial transient phase during which the capsule deforms very quickly, over a wide range of Ca, size ratio (a/H), and viscosity ratio (λ).

Dependence of the migration velocity with respect to Ca, size ratio and capsule location is studied and compared with the small-deformation theory for liquid drops, and capsules with Hookean membrane. Unlike the linear theory, migration velocity shows a non-linear dependence on Ca and capsule location. The linear theory is seen to overpredict the migration velocity, and underpredict the slip velocity at higher Ca. This departure could be due to both large deformation and small wall distance. Interestingly, however, the linear dependence on $(a/H)^3$ as predicted by the theory appears to be valid even in the limit of large deformation, as shown by the simulation results. Using the present numerical results, and the analytical results of Shapira and Haber (1988), we then present a correlation that can reasonably predict migration velocity of a capsule for moderate values of a/H and Ca. Unlike the prediction for liquid drops (Chan and Leal, 1979), capsules are observed to migrate toward the center for $0.2 \leqslant \lambda \leqslant 5$ range considered here.

Results presented here depict the effect of curvature in the velocity profile, as well as the wall effects. For the undisturbed Poiseuille flow considered here, it is difficult to isolate the wall effect and the curved velocity profile due to the way the computational problem is set up. In order to isolate the wall effect using the present computational setup, one can consider a linear shear flow where the capsule can be placed away from the wall without any change in the shear rate. Identifying such wall effects in the case of large deformation of a capsule is left for future investigation.

While experimental data on lateral migration of single liquid drop are available in the literature (e.g. Smart and Leighton, 1991), we are not aware of similar data on capsule migration. Indeed there are experimental results available on capsule deformation in linear shear flow, and on single-file motion (see Section 1). Results on lateral migration of erythrocytes in tube or channel flow are not abundant. Experiments by Goldsmith and co-workers (e.g. Goldsmith, 1971) was mentioned earlier. Recently, Secomb et al. (2007) presented two-dimensional simulation on erythrocyte migration in 8-μm capillary. The simulation result was verified qualitatively by experimental data on cell trajectories observed in microvessels of the rat mesentery. The results presented in this article are, however, for three-dimensional capsules in a planar flow, and hence cannot be directly compared with their numerical or experimental data. It appears that migration experiments using spherical capsules are necessary.

Acknowledgments

This work is supported in part by grants from National Science Foundation (BES-0603035, CTS-0625936). Computational support from the National Center for Supercomputing Applications, Illinois, and San Diego Supercomputing Center is acknowledged. We also thank the referees for their comments.

References

Barthes-Biesel, D., 1980. Motion of a spherical microcapsule freely suspended in a linear shear flow. J. Fluid Mech. 100, 831–853.

Barthes-Biesel, D., Chim, V., 1981. Constitutive equation of a dilute suspension of spherical microcapsules. Int. J. Multiphase Flow 7, 473–493.

Barthes-Biesel, D., Rallison, J.M., 1981. The time-dependent deformation of a capsule freely suspended in a linear shear flow. J. Fluid Mech. 113, 251–267.

Barthes-Biesel, D., Sgaier, H., 1985. Role of membrane viscosity in the orientation and deformation of a spherical capsule suspended in shear flow. J. Fluid Mech. 160, 119–135.

Barthes-Biesel, D., Diaz, A., Dhenin, E., 2002. Effect of constitutive laws for two-dimensional membranes on flow-induced capsule deformation. J. Fluid Mech. 460, 211–222.

Borhan, A., Gupta, N.R., 2003. Capsule motion and deformation in tube and channel flow. In: Pozrikidis, C. (Ed.), Modeling and Simulation of Capsules and Biological Cells. Chapman & Hall/CRC, Boca Raton, FL.

Brenner, B., 1970. Pressure drop due to the motion of neutrally buoyant particles in duct flows. J. Fluid Mech. 43, 641–660.

Breyiannis, G., Pozrikidis, C., 2000. Simple shear flow of suspensions of elastic capsules. Theor. Comput. Fluid Dynam. 13, 327–347.

Chaffey, C.E., Brenner, H., mason, S.G., 1967. Particle motions in sheared suspensions XXII. Wall migration theoretical. Rheol. Acta 4, 64–75.

Chan, P.C.-H., Leal, L.G., 1979. The motion of a deformable drop in a second-order fluid. J. Fluid Mech. 92, 131–170.

Chan, P.C.-H., Leal, L.G., 1981. An experimental study of drop migration in shear flow between concentric cylinders. Int. J. Multiphase Flow 7, 83–94.

Chang, K.S., Olbricht, W.L., 1993. Experimental studies of the deformation of a synthetic capsule in extensional flow. J. Fluid Mech. 250, 587–608.

Charrier, J.M., Shrivastava, S., Wu, R., 1989. Free and constrained inflation of elastic membranes in relation to thermoforming-non-axisymmetric problems. J. Strain Anal. 24, 55–74.

Coulliette, C., Pozrikidis, C., 1998. Motion of an array of drops through a cylindrical tube. J. Fluid Mech. 358, 1–28.

Diaz, A., Pelekasis, N., Barthes-Biesel, D., 2000. Transient response of a capsule subjected to varying flow conditions: effect of internal fluid viscosity and membrane elasticity. Phys. Fluids 12, 948–958.

Diaz, A., Barthes-Biesel, D., Pelekasis, N., 2001. Effect of membrane viscosity on the dynamic response of an axisymmetric capsule. Phys. Fluids 13, 3835–3839.

Eggleton, C.D., Popel, A.S., 1998. Large deformation of red blood cell ghosts in a simple shear flow. Phys. Fluids 10, 1834–1845.

Goldman, A.J., Cox, R.G., Brenner, H., 1967. Slow viscous motion of a sphere parallel to a plane wall: II Couette flow. Chem. Eng. Sci. 22, 653–660.

Goldsmith, H.L., 1971. Red cell motions and wall interactions in tube flow. Federation Proc. 30, 1578–1590.

Goldsmith, H.L., Mason, S.G., 1962. The flow of suspensions through tubes. I. Single spheres rods and disks. J. Colloid Sci. 17, 448–476.

Griggs, A.J., Zinchenko, A.Z., Davis, R.H., 2007. Low-Reynolds-number motion of a deformable drop between two parallel plane walls. Int. J. Multiphase Flow 33, 182–206.

Gutcho, M.H., 1979. Microcapsules and Other Capsules. Noyes Data Corporation, Park Ridge, NJ.

Helmy, A., Barthes-Biesel, D., 1982. Migration of a spherical capsule freely suspended in an unbounded parabolic flow. J. Mecanique theorique appliquee 1, 859–880.

Hiller, W., Kowalewski, T.A., 1987. An experimental study of the lateral migration of a droplet in a creeping flow. Exp. Fluids 5, 43–48.

Ho, B.P., Leal, L.G., 1974. Inertial migration of rigid spheres in two-dimensional unidirectional flows. J. Fluid Mech. 65, 365–400.

Karnis, A., Goldsmith, H.L., Mason, S.G., 1963. Axial migration of particles in Poiseuille flow. Nature 200, 159–160.

Kwak, S., Pozrikidis, C., 2001. Effect of membrane bending stiffness on the axisymmetric deformation of capsules in uniaxial extensional flow. Phys. Fluids 13, 1234–1244.

Karnis, A., Mason, S.G., 1967. Particle motions in sheared suspensions. XXIII. Wall migration of fluid drops. J. Colloid Interf. Sci. 24, 164–169.

Lac, E., Barthes-Biesel, D., Pelekasis, N.A., Tsamopoulos, J., 2004. Spherical capsules in three-dimensional unbounded Stokes flows: effect of the membrane constitutive law and onset of buckling. J. Fluid Mech. 516, 303–334.

Lac, E., Barthes-Biesel, D., 2005. Deformation of a capsule in simple shear flow: effect of membrane prestress. Phys. Fluids 17, 072105.

Lac, E., Morel, A., Barthes-Biesel, D., 2007. Hydrodynamic interaction between two identical capsules in simple shear flow. J. Fluid Mech. 573, 149–169.

Leyrat-Maurin, A., Barthes-Biesel, D., 1994. Motion of a deformable capsule through a hyperbolic constriction. J. Fluid Mech. 279, 135–163.

Li, X.Z., Barthes-Biesel, D., Helmy, A., 1988. Large deformations and burst of a capsule freely suspended in an elongational flow. J. Fluid Mech. 187, 179–196.

Li, X., Pozrikidis, C., 2000. Wall-bounded and channel flow of suspensions of liquid drops. Int. J. Multiphase Flow 26, 1247–1279.

Li, X., Sarkar, K., 2008. Front-tracking simulation of deformation and buckling instability of a liquid capsule enclosed by an elastic membrane. J. Comput. Phys 227, 4998–5018.

Magnaudet, J., 2003. Small inertial effects on a spherical bubble, drop or particle moving near a wall in a time-dependent linear flow. J. Fluid Mech. 485, 115–142.

Magnaudet, J., Takagi, S., Legendre, D., 2003. Drag deformation and lateral migration of a buoyant drop moving near a wall. J. Fluid Mech. 476, 115–157.

Marella, S.V., Udaykumar, H.S., 2004. Computational analysis of the deformability of leukocytes and modeled with viscous and elastic structural components. Phys. Fluids 16, 244–264.

Mortazavi, S., Tryggvason, G., 2000. A numerical study of the motion of drops in Poiseuille flow. Part 1. Lateral migration of one drop. J. Fluid Mech. 411, 325–350.

Peskin, C.S., 1977. Numerical analysis of blood flow in the heart. J. Comput. Phys. 25, 220–233.

Pozrikidis, C., 1995. Finite deformation of liquid capsules enclosed by elastic membranes in simple shear flow. J. Fluid Mech. 297, 123–152.

Pozrikidis, C., 2001. Effect of bending stiffness on the deformation of liquid capsules in simple shear flow. J. Fluid Mech. 440, 269–291.

Pozrikidis, C., 2003. Modeling and Simulation of Capsules and Biological Cells. Chapman & Hall/CRC, Boca Raton, FL.

Pozrikidis, C., 2005. Numerical simulation of cell motion in tube flow. Ann. Biomed. Eng. 33, 165–178.

Queguiner, C., Barthes-Biesel, D., 1997. Axisymmetric motion of capsules through cylindrical channels. J. Fluid Mech. 348, 349–376.

Ramanujan, S., Pozrikidis, C., 1998. Deformation of liquid capsules enclosed by elastic membranes in simple shear flow: large deformations and the effect of fluid viscosities. J. Fluid Mech. 361, 117–143.

Rehage, H., Husmann, M., Walter, A., 2002. From two-dimensional model networks to microcapsules. Rheol. Acta 41, 292–306.

Risso, F., Colle-Paillot, F., Zagzoule, M., 2006. Experimental investigation of a bioartificial capsule flowing in a narrow tube. J. Fluid Mech. 547, 149–174.

Secomb, T.W., Styp-Rekowska, B., Pries, A.R., 2007. Two-dimensional simulation of red blood cell deformation and lateral migration in microvessels. Ann. Biomed. Eng. 35, 755–765.

Shapira, M., Haber, S., 1988. Low Reynolds number motion of a droplet between two parallel plates. Int. J. Multiphase Flow 14, 483–506.

Shapira, M., Haber, S., 1990. Low Reynolds number motion of a droplet in shear flow including wall effects. Int. J. Multiphase Flow 16, 305–321.

Smart, J.R., Leighton, D.T., 1991. Measurement of the drift of a droplet due to the presence of a plane. Phys. Fluids 3, 21–31.

Shrivastava, S., Tang, J., 1993. Large deformation finite element analysis of non-linear viscoelastic membranes with reference to thermoforming. J. Strain Anal. 28, 31–43.

Tryggvason, G., Bunner, B., Esmaeeli, A., Juric, D., Al-Rawahi, N., Tauber, W., Han, J., Nas, S., Jan, Y.-J., 2001. A front tracking method for the computations of multiphase flow. J. Comput. Phys. 169, 708–759.

Uijttewaal, W.S.J., Nijhof, E.J., Heethaar, R.M., 1993. Droplet migration, deformation, and orientation in the presence of a plane wall – A numerical study compared with analytical theories. Phys. Fluids 5, 819–833.

Uijttewaal, W.S.J., Nijhof, E.J., 1995. The motion of a droplet subjected to linear shear flow including the presence of a wall. J. Fluid Mech. 302, 45–60.

Unverdi, S.O., Tryggvason, G., 1992. A front-tracking method for viscous, incompressible multi-fluid flows. J. Comput. Phys. 100, 25–37.

Walter, A., Rehage, H., Leonhard, H., 2001. Shear-induced deformations of microcapsules: shape oscillations and membrane folding. Colloid. Surf. A – Physicochem. Eng. Asp. 183, 123–132.